

THE ACCRETING BLACK HOLE SWIFT J1753.5–0127 FROM RADIO TO HARD X-RAY

JOHN A. TOMSICK¹, FARID RAHOUI^{2,3}, MARI KOLEHMAINEN⁴, JAMES MILLER-JONES⁵, FELIX FÜRST⁶, KAZUTAKA YAMAOKA^{7,8}, HIROSHI AKITAYA⁹, STÉPHANE CORBEL^{10,11}, MICKAEL CORIAT¹², CHRIS DONE¹³, POSHAK GANDHI¹⁴, FIONA A. HARRISON⁶, KUIYUN HUANG¹⁵, PHILIP KAARET¹⁶, EMRAH KALEMCI¹⁷, YUKA KANDA¹⁸, SIMONE MIGLIARI¹⁹, JON M. MILLER²⁰, YUKI MORITANI^{8,21}, DANIEL STERN²², MAKOTO UEMURA⁸, YUJI URATA²³

Accepted by ApJ

ABSTRACT

We report on multi-wavelength measurements of the accreting black hole Swift J1753.5–0127 in the hard state at low luminosity ($L \sim 2.7 \times 10^{36}$ erg s⁻¹ assuming a distance of $d = 3$ kpc) in 2014 April. The radio emission is optically thick synchrotron, presumably from a compact jet. We take advantage of the low extinction ($E(B-V) = 0.45$ from earlier work) and model the near-IR to UV emission with a multi-temperature disk model. Assuming a black hole mass of $M_{\text{BH}} = 5 M_{\odot}$ and a system inclination of $i = 40^{\circ}$, the fits imply an inner radius for the disk of $R_{\text{in}}/R_g > 212 d_3 (M_{\text{BH}}/5 M_{\odot})^{-1}$, where R_g is the gravitational radius of the black hole, and d_3 is the distance to the source in units of 3 kpc. The outer radius is $R_{\text{out}}/R_g = 90,000 d_3 (M_{\text{BH}}/5 M_{\odot})^{-1}$, which corresponds to $6.6 \times 10^{10} d_3$ cm, consistent with the expected size of the disk given previous measurements of the size of the companion’s Roche lobe. The 0.5–240 keV energy spectrum measured by *Swift*/XRT, *Suzaku* (XIS, PIN, and GSO), and *NuSTAR* is relatively well characterized by an absorbed power-law with a photon index of $\Gamma = 1.722 \pm 0.003$ (90% confidence error), but a significant improvement is seen when a second continuum component is added. Reflection is a possibility, but no iron line is detected, implying a low iron abundance. We are able to fit the entire (radio to 240 keV) spectral energy distribution (SED) with a multi-temperature disk component, a Comptonization component, and a broken power-law, representing the emission from the compact jet. The broken power-law cannot significantly contribute to the soft X-ray emission, and this may be related to why Swift J1753.5–0127 is an outlier in the radio/X-ray correlation. The broken power-law (i.e., the jet) might dominate above 20 keV, which would constrain the break frequency to be between 2.4×10^{10} Hz and 3.6×10^{12} Hz. Although the fits to the full SED do not include significant thermal emission in the X-ray band, previous observations have consistently seen such a component, and we find that there is evidence at the $3.1\text{-}\sigma$ level for a disk-blackbody component with a temperature of $kT_{\text{in}} = 150_{-20}^{+30}$ eV and an inner radius of $5\text{--}14 R_g$. If this component is real, it might imply the presence of an inner optically thick accretion disk in addition to the strongly truncated ($R_{\text{in}} > 212 R_g$) disk. We also perform X-ray timing analysis, and the power spectrum is dominated by a Lorentzian component with $\nu_{\text{max}} = 0.110 \pm 0.003$ Hz and $\nu_{\text{max}} = 0.16 \pm 0.04$ Hz as measured by XIS and XRT, respectively.

Subject headings: accretion, accretion disks — black hole physics — stars: individual (Swift J1753.5–0127)
 — X-rays: stars — X-rays: general

1. INTRODUCTION

Most accreting stellar-mass black holes in binary systems exhibit large changes in luminosity over time, ranging from a substantial fraction of the Eddington limit (L_{Edd}) to $\sim 10^{-8}$ or $\sim 10^{-9} L_{\text{Edd}}$. In addition to changes in luminosity, these

¹ Space Sciences Laboratory, 7 Gauss Way, University of California, Berkeley, CA 94720-7450, USA

² European Southern Observatory, Karl Schwarzschild-Strasse 2, 85748 Garching bei Munchen, Germany

³ Department of Astronomy, Harvard University, 60 Garden Street, Cambridge, MA 02138, USA

⁴ Astrophysics, Department of Physics, University of Oxford, Keble Road, Oxford OX1 3RH, UK

⁵ International Centre for Radio Astronomy Research, Curtin University, GPO Box U1987, Perth, WA 6845, Australia

⁶ California Institute of Technology, 1200 East California Boulevard, Pasadena, CA 91125, USA

⁷ Solar-Terrestrial Environment Laboratory, Nagoya University, Furocho, Chikusa-ku, Nagoya, Aichi 464-8601, Japan

⁸ Division of Particle and Astrophysical Science, Department of Physics, Nagoya University, Furo-cho, Chikusa-ku, Nagoya, Aichi 464-8602, Japan

⁹ Hiroshima Astrophysical Science Center, Hiroshima University, Kagamiyama, Higashi-Hiroshima, Hiroshima 739-8526, Japan

¹⁰ Laboratoire AIM (CEA/IRFU - CNRS/INSU - Université Paris Diderot), CEA DSM/IRFU/Sap, F-91191 Gif-sur-Yvette, France

¹¹ Station de Radioastronomie de Nançay, Observatoire de Paris, PSL Research University, CNRS, Univ. Orléans, OSUC, 18330 Nançay, France

¹² Institut de Recherche en Astrophysique et Planétologie (IRAP), 9 Avenue du Colonel Roche, 31028 Toulouse Cedex 4, France

¹³ Department of Physics, University of Durham, South Road, Durham DH1 3LE, UK

¹⁴ School of Physics & Astronomy, University of Southampton, Highfield, Southampton SO17 1BJ, UK

¹⁵ Department of Mathematics and Science, National Taiwan Normal University, Lin-kou District, New Taipei City 24449, Taiwan

¹⁶ Department of Physics and Astronomy, University of Iowa, Van Allen Hall, Iowa City, IA 52242, USA

¹⁷ Sabanci University, Orhanli-Tuzla, Istanbul, 34956, Turkey

¹⁸ Department of Physical Science, Hiroshima University, Kagamiyama, Higashi-Hiroshima 739-8526, Japan

¹⁹ European Space Astronomy Centre, Apartado/P.O. Box 78, Villanueva de la Canada, E-28691 Madrid, Spain

²⁰ Department of Astronomy, University of Michigan, 500 Church Street, Ann Arbor, MI 48109-1042, USA

²¹ Kavli Institute for the Physics and Mathematics of the Universe (WPI), The University of Tokyo, 5-1-5, Kashiwanoha, Kashiwa, 277-8583, Japan

²² Jet Propulsion Laboratory, California Institute of Technology, 4800 Oak Grove Drive, Pasadena, CA 91109, USA

²³ Institute of Astronomy, National Central University, Chung-Li 32054, Taiwan

systems show other observational changes, including transitions between distinct spectral states that are similar from system-to-system (e.g., McClintock & Remillard 2006; Belloni 2010). The thermal dominant (or soft) state has a strong thermal component from an optically thick accretion disk in the X-ray spectrum. In the hard state on the other hand, this component contributes a lower fraction of the flux in the X-ray band. The drop in flux is partly due to a decrease in the temperature of the component (Kalemci et al. 2004), moving its peak into the ultraviolet where it is difficult to measure due to interstellar absorption. While the soft thermal X-ray emission weakens, there is a strong increase in the hard X-rays, and the X-ray spectrum in the hard state is dominated by a power-law, which often has an exponential cutoff above 50–100 keV (Grove et al. 1998; Gilfanov & Merloni 2014).

Accreting black holes also emit in the radio band when they are in the hard state, and this is due to a powerful compact jet (Corbel et al. 2000; Fender 2001). At radio frequencies, the spectrum is dominated by a partially self-absorbed synchrotron component that has a flat or rising spectrum ($F_\nu \propto \nu^\alpha$, where $\alpha \gtrsim 0$). The jet spectrum changes slope above the break frequency, ν_{break} , becoming steeper because the frequency is sufficiently high that the entire jet is optically thin. In some cases, the measurement of ν_{break} has been constrained to be in the infrared (IR) to optical (Corbel & Fender 2002; Gandhi et al. 2011; Rahoui et al. 2011; Russell et al. 2013a,b, 2014), but its measurement can be complicated because of the other emission components (e.g., from the accretion disk or the optical companion) and also because the jet spectrum is likely significantly more complicated than a simple broken power-law (Markoff, Nowak & Wilms 2005; Migliari et al. 2007).

In the hard state, it is clear that there is a strong connection between the X-ray and radio emission. The fluxes in the two bands are correlated (Corbel et al. 2000, 2003; Gallo, Fender & Pooley 2003; Corbel, Koerding & Kaaret 2008; Corbel et al. 2013; Gallo et al. 2014), and while early studies suggested that all black hole sources might lie on the same correlation line, observations of more systems have shown that this is not the case (Jonker et al. 2010; Coriat et al. 2011). A current topic of debate is whether all sources lie on two correlation lines, one track for standard sources and one for outliers, or if there is a continuum of different tracks (Coriat et al. 2011; Corbel et al. 2013; Gallo et al. 2014). Another topic is how much, if any, of the X-ray emission originates in the jet. While the most typical hard state spectrum with an exponential cutoff is well described by thermal Comptonization, and it has been argued that it is unlikely that this emission is due to synchrotron emission from a jet (Zdziarski et al. 2003), some black hole spectra appear to have multiple high-energy continuum components (Joinet et al. 2007; Rodriguez et al. 2008; Bouchet et al. 2009; Droulans et al. 2010; Russell et al. 2010), and a jet origin is not ruled-out. In fact, Cygnus X-1 often shows two high-energy components in the hard state, including an MeV component (McConnell et al. 2000; Rahoui et al. 2011; Zdziarski, Lubiński & Sikora 2012), and the detection of strong polarization at >400 keV favors a synchrotron origin (Laurent et al. 2011; Jourdain et al. 2012).

The fact that a jet is present in the hard state and that there is some connection between the disk and the jet leads to the question of what we know about the disk properties. The main question regarding the optically thick disk concerns the location of the inner radius (R_{in}). One idea is that the black hole states are essentially determined by the mass accretion rate

and R_{in} (Esin, McClintock & Narayan 1997), with sources entering the hard state because of an increase in R_{in} . However, X-ray observations of sources in the bright hard state seem to contradict this since relativistically smeared reflection components are seen from some systems that imply that the disk remains close to the innermost stable circular orbit (ISCO; Blum et al. 2009; Reis et al. 2011; Miller et al. 2012; Fabian et al. 2012). In addition, thermal component modeling has led to similar conclusions (Reis, Fabian & Miller 2010). While photon pile-up in CCD spectra has sparked some debate about iron line results (Miller et al. 2006; Done & Diaz Trigo 2010; Miller et al. 2010), more recent observations with the *Nuclear Spectroscopic Telescope Array* (*NuSTAR*) confirm strongly broadened and skewed iron lines in the bright hard state for GRS 1915+105 (Miller et al. 2013), GRS 1739–278 (Miller et al. 2015), GX 339–4 (Fürst et al. 2015), and Cygnus X-1 (Parker et al. 2015). For the case of GRS 1739–278, the luminosity is $\sim 5\%$ L_{Edd} , and the inferred inner radius is $< 12 R_g$ (Miller et al. 2015), where $R_g = GM_{\text{BH}}/c^2$ and G is the gravitational constant, M_{BH} is the black hole mass, and c is the speed of light. Significantly truncated disks have been reported for the hard state at intermediate and low luminosities using reflection component modeling (Tomsick et al. 2009; Shidatsu et al. 2011; Plant et al. 2015) and also by modeling the thermal component from the optically thick disk (Gierliński, Done & Page 2008; Cabanac et al. 2009).

To investigate questions related to the accretion geometry and the relationship between the disk and the jet, we performed multi-wavelength observations of the accreting black hole Swift J1753.5–0127 in the hard state. This system was first discovered in outburst in 2005 (Palmer et al. 2005), and it is very unusual in that it has been bright in X-rays for almost a decade. The optical light curve shows a 3.2 hour modulation, which has been interpreted as a superhump period (a modulation due to tidal stresses on a precessing, elliptical accretion disk), suggesting that the orbital period is somewhat smaller than this (Zurita et al. 2008). From radial velocity measurements, Neustroev et al. (2014) find a 2.85 hour signal, which is likely the true orbital period. Thus, Swift J1753.5–0127 has one of the shortest orbital periods of any known black hole binary. Although the mass of the black hole in Swift J1753.5–0127 is still debated since there has not been an opportunity to obtain a radial velocity measurement for the companion star with the system in quiescence, Neustroev et al. (2014) argue that the mass is relatively low, $M_{\text{BH}} < 5 M_\odot$, and we adopt a black hole mass of $5 M_\odot$ for calculations in this paper.

Swift J1753.5–0127 is also unusual in that it has a low level of extinction, due in part to it being somewhat out of the plane with Galactic coordinates of $l = 24.9^\circ$ and $b = +12.2^\circ$. Froning et al. (2014) obtained UV measurements showing that $E(B-V) = 0.45$, and we confirm this value in a companion paper (Rahoui et al., submitted to ApJ). It is not entirely clear whether the system is relatively nearby or in the Galactic halo as there is a large range of possible distances, $d = 1\text{--}10$ kpc (Cadolle Bel et al. 2007; Zurita et al. 2008; Froning et al. 2014). Froning et al. (2014) provide evidence that the UV emission from Swift J1753.5–0127 in the hard state comes from an accretion disk, and they calculate distance upper limits that depend on M_{BH} , assuming that the mass accretion rate is less than 5% L_{Edd} . For $M_{\text{BH}} = 5 M_\odot$, the upper limit is 2.8–3.7 kpc, depending on the inclination of the system, and we use a fiducial distance of 3 kpc for the calculations in this paper.

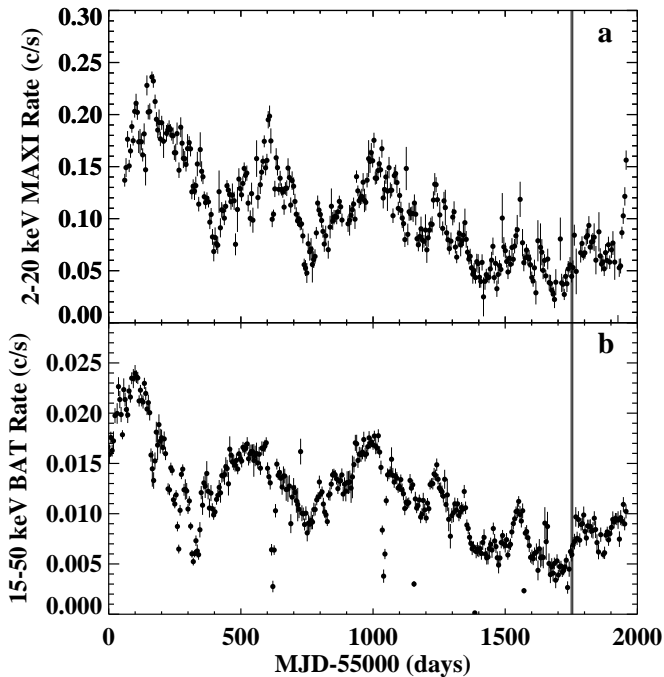


FIG. 1.— *MAXI* (a) and *Swift*/BAT (b) light curves in the 2–20 keV and 15–50 keV bands for Swift J1753.5–0127 between mid-2009 and mid-2014. The vertical lines mark the start and stop times of the observations used in this work (2014 April 2–8).

Swift J1753.5–0127 has been extensively observed in the radio band, and is one of the clearest examples of a source that is an outlier in the radio/X-ray correlation plot (Soleri et al. 2010; Corbel et al. 2013). The location on the plot depends on the assumed distance, and the previous work has assumed a source distance of 8 kpc. While we are adopting a significantly smaller distance, Soleri et al. (2010) considered how distance affects the the radio underluminosity, which is a measure of how far a source is from the standard correlation. Soleri et al. (2010) show that a smaller distance moves the source farther from the standard correlation (see also Jonker et al. 2004). Thus, the fact that recent work suggests that Swift J1753.5–0127 is closer than early estimates only strengthens the conclusion that the source is an outlier.

For this work, we have carried out a large campaign to observe Swift J1753.5–0127 in the hard state with radio, near-IR, optical, UV, and X-ray observations as described in Section 2. In the X-ray, data were obtained with *NuSTAR*, *Suzaku*, and *Swift*/XRT. The observations occurred when the flux level was close to the minimum brightness this source has had in the ~ 10 years since its discovery (see Figure 1). The low flux level (and presumably mass accretion rate) may cause changes in the properties of the accretion disk or jet compared to previous observations at higher flux levels. In Section 3, we perform spectral analysis for the different energy ranges (radio, near-IR to UV, and X-ray) separately and then also as a combined radio to X-ray Spectral Energy Distribution (SED). We also produce an X-ray power spectrum for timing analysis. We discuss the results in Section 4, and then provide conclusions in Section 5.

2. OBSERVATIONS AND DATA REDUCTION

The observations that we obtained in 2014 April are listed in Table 1, and more details about the observation times are shown in Figure 2. The X-ray flux was rising very slowly during the observation, and this is seen especially clearly in the *Suzaku*/XIS light curve (Figure 2). We provide more details about the observatories used and how the data were processed in the following.

2.1. Radio

We observed Swift J1753.5–0127 with the Karl G. Jansky Very Large Array (VLA) on 2014 April 5 (MJD 56752) from 11:00–13:00 UT with the array in its most-extended A-configuration. We split the observing time between the 4–8 and 18–26-GHz observing bands. In the lower 4–8 GHz band, we split the available bandwidth into two 1024-MHz basebands, centered at 5.25 and 7.45 GHz. Each baseband was split into eight 128-MHz spectral windows, each of which comprised sixty-four 2-MHz channels. The higher-frequency 18–26 GHz band was fully covered by four 2048-MHz basebands, each comprising sixteen 128-MHz sub-bands made up of sixty-four 2-MHz channels. After accounting for calibration overheads, the total on-source integration times for Swift J1753.5–0127 were 25.3 minutes in the 4–8-GHz band and 29.1 minutes in the 18–26-GHz band.

The data were reduced using version 4.2.0 of the Common Astronomy Software Application (CASA; McMullin et al. 2007). We applied a priori calibration to account for updated antenna positions and gain variations with changing elevation or correlator configuration, and corrected the 18–26-GHz data for opacity effects. We edited out any data affected by antenna shadowing before Hanning smoothing the data and removing any radio frequency interference. At all frequencies we used 3C286 to calibrate the instrumental frequency response, and to set the amplitude scale according to the default Perley-Butler 2010 coefficients implemented in the CASA task `SETJY`. We used J1743-0350 as a secondary calibrator to determine the time-varying complex gains arising from both atmospheric and instrumental effects.

The calibrated data on Swift J1753.5–0127 were averaged by a factor of four in frequency to reduce the raw data volume, and then imaged using Briggs weighting with a robust parameter of 1 to achieve the best compromise between sensitivity and sidelobe suppression. When imaging, we used the multi-frequency synthesis algorithm as implemented in CASA’s `CLEAN` task, choosing two Taylor terms to account for the frequency dependence of source brightness. The source was clearly detected in all frequency bands, with an inverted spectrum ($\alpha > 0$, where the flux density S_ν varies as a function of frequency ν as $S_\nu \propto \nu^\alpha$). To better constrain the radio spectrum, we split each frequency band into four frequency bins (of width 1024 MHz at 4–8 GHz, and 2048 MHz at 18–26 GHz where the intrinsic sensitivity per unit frequency is lower). We measured the source brightness in each frequency bin by fitting an elliptical Gaussian to the brightness distribution in the image plane. Swift J1753.5–0127 appeared unresolved at all frequencies.

Swift J1753.5–0127 was also observed with the Mullard Radio Astronomy Observatory’s Arcminute Microkelvin Imager (AMI) Large Array (Zwart et al. 2008) on two occasions during the coordinated multi-wavelength campaign between 2014 April 4–5. These ~ 4 -hour observations were taken at the times given in Table 1 with a central frequency of 15.4 GHz. The AMI Large Array consists of eight 13-m dishes, with the full frequency band of 12–17.9 GHz being di-

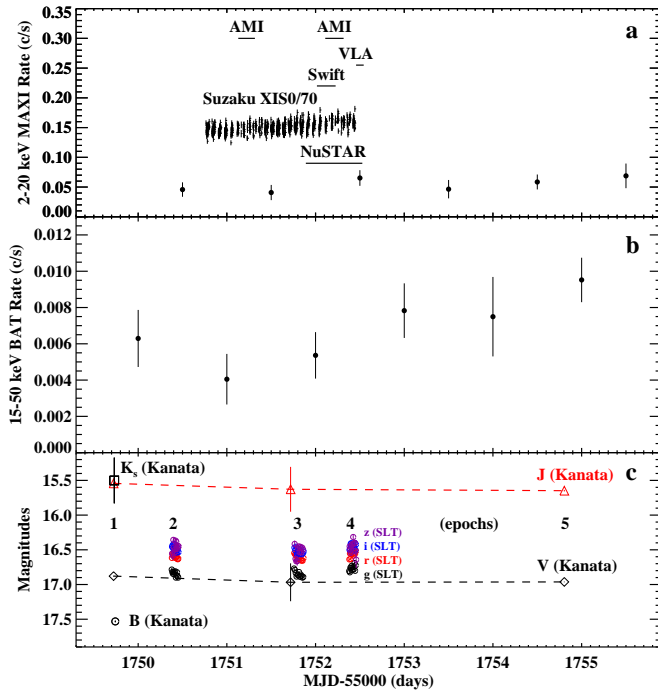


FIG. 2.— (a) The filled circles show the *MAXI* light curve over the time of the observations (2014 April 2–8). The times of the AMI, VLA, *Swift*/XRT, *Suzaku*, and *NuSTAR* observations are indicated. Also, the 1–12 keV light curve for *Suzaku*/XIS0 is shown (the actual count rate divided by 70). (b) The *Swift*/BAT light curve over the time of the observations. (c) The optical and near-IR magnitudes measured at the Kanata and SLT telescopes.

vided into eight 0.75 GHz bandwidth channels. Channels 1–2 and 8 were ignored due to lower response in those frequency ranges and the expected high level of interference from satellites due to the low elevation of the source. The primary beam FWHM is ≈ 6 arcmin at 16 GHz.

The AMI data were reduced using the semi-automated pipeline procedure described in Staley et al. (2013), which uses the AMI software tool *REDUCE* to automatically flag for interference, shadowing and hardware errors, calibrate the gain, and synthesize the frequency channels to produce visibility data in *uv-FITS* format (see Staley et al. 2013, for more details). However, the low elevation and the radio-quiet nature of the source resulted in high noise levels in the reduced images, and thus the two observations were concatenated to maximize the signal-to-noise. The concatenated dataset was then imaged in *CASA*, where the *CLEAN* task was used to produce the combined frequency image, and the flux density was measured by fitting a Gaussian model to the source in the radio map using the *MIRIAD* task *IMFIT*. The error on the concatenated flux density was calculated as

$$\sigma = \sqrt{(0.05S_\nu)^2 + \sigma_{\text{fit}}^2 + \sigma_{\text{rms}}^2}$$

following AMI Consortium et al. (2012), with a 5% absolute calibration error added to the fitting error σ_{fit} calculated in *IMFIT*. The source concatenated flux density was measured at $290 \pm 50 \mu\text{Jy}$.

2.2. Ground-Based Optical and Near-IR

Kanata is a 1.5 m telescope at the Higashi-Hiroshima Observatory. Photometric observations were performed for this study on three nights (MJD 56749, 56751, and 56754) with

the *B*, *V*, *J*, and *K_s* bands using the HONIR instrument (Sakimoto et al. 2012; Akitaya et al. 2014) attached to Kanata. The individual frame exposure times were 75, 136, 120, and 60 s in *B*, *V*, *J*, *K_s*-bands, respectively. The data reduction was performed in the standard manner: the bias and dark images were subtracted from all images, and then the images were flat-fielded. The magnitudes of the object and comparison stars were measured using PSF photometry. For the *B*, *V*, and *J*-band photometry, we used the comparison star located at R.A.=17^h53^m25.^s275, Decl.=−01°27′30.″05 (J2000.0), which has magnitudes of *B* = 17.62, *V* = 16.66, and *J* = 14.468 (Zurita et al. 2008; Skrutskie et al. 2006). For the *K_s*-band photometry, we used the comparison star at R.A.=17^h53^m25.^s853, Decl.=−01°26′17.″00 (J2000.0), for which *K_s* = 11.132 (Skrutskie et al. 2006).

We also conducted optical *g'*, *r'*, *i'*, and *z'* band monitoring observations with the Lulin 41 cm Super-Light Telescope (SLT), which is located in Taiwan, on three nights in 2014 April (see Table 1). Photometric images with 180 s exposures were obtained using the U42 CCD camera. We performed the dark-subtraction and flat-fielding correction using the appropriate calibration data with the *IRAF* package. Photometric calibrations were made with the Pan-STARRS1 3π catalogs (Magnier et al. 2013; Schlafly et al. 2012; Tonry et al. 2012). The *DAOPHOT* package was used to perform the aperture photometry of the multi-band images.

2.3. Swift

The *Swift* satellite (Gehrels et al. 2004) includes two pointed instruments, the X-ray Telescope (XRT; Burrows et al. 2005) and the Ultra-Violet/Optical Telescope (UVOT; Roming et al. 2005), and we used data from both instruments from ObsID 00080730001 in this work. We performed the XRT data reduction using *HEASOFT* v6.15.1 and the 2013 March version of the XRT calibration data base (CALDB), and made event lists using *xrtpipeline*. The XRT instrument was in Windowed Timing mode to avoid photon pile-up. For spectral analysis, we extracted photons from within 47'' of the *Swift* J1753.5–0127 position, and made a background spectrum from a region away from the source. We measured an XRT source count rate of 7.7 c/s in the 0.5–10 keV band during the 2.4 ks observation. We used the appropriate response file from the CALDB (swxwt0to2s6_20010101v015.rmf) and produced a new ancillary response file using *xrtmkarf* and the exposure map generated by *xrtpipeline*. We binned the 0.5–10 keV spectra so that each bin has a signal-to-noise of 10.

For UVOT, we obtained photometry in six filters (*v*, *b*, *u*, *uvw1*, *uvw2*, and *uvw3*) during the observation. For each filter, we produced an image using *uvotimsum* and made a source region with a radius of 5'' and a background region from a source-free region. Then, we used *uvotsource* to perform the photometry and calculate the magnitude and flux of *Swift* J1753.5–0127 for each filter.

Swift also includes the wide field of view (FoV) Burst Alert Telescope (BAT), and we use data from BAT to study the long-term 15–50 keV flux (see Figures 1 and 2).

2.4. NuSTAR

The *Nuclear Spectroscopic Telescope Array* (*NuSTAR*; Harrison et al. 2013) consists of two co-aligned X-ray telescopes, FPMA and FPMB, sensitive between 3–79 keV. To reduce the data, we used *nupipeline* v.1.3.1 as distributed with *HEA-*

SOFT 6.15.1. During our analysis, an updated version became available, but we carefully checked that it does not influence our results. We extracted the source spectrum from a circular region with $90''$ radius centered on the J2000 coordinates. Due to the triggered readout of the detectors, pile-up is not a concern for *NuSTAR*. The background was extracted from a circular region with a $170''$ radius at the other end of the FoV. Small systematic changes of the background over the FoV can be neglected, as Swift J1753.5–0127 is a factor of six brighter than the background, even at 70 keV. The spectrum includes data from two *NuSTAR* ObsIDs. We reduced both ObsIDs separately and added the resulting spectra and response files using `addascaspec`. The resulting total exposure time is given in Table 1.

2.5. *Suzaku*

For *Suzaku*, we used data from the X-ray Imaging Spectrometers (XISs; Koyama et al. 2007) and from the Hard X-ray Detector (HXD; Takahashi et al. 2007) PIN diode detector, and the HXD gadolinium silicate crystal detector (GSO). The XIS has three CCD detectors (XIS0, XIS1, and XIS3) that operate in the 0.4–12 keV bandpass. We produced event lists for each detector using `aepipeline` and merged the event lists taken in the 3×3 and 5×5 CCD editing modes. We ran `aeattcor2` and `xiscoord` on each of the merged event files to update the attitude correction because this is important for the pile-up estimate, which we calculated using `pileest`. We extracted source spectra using a $4'$ -radius circle with the inner $22''$ removed due to pile-up at a level of $>4\%$ in the core of the point spread function (PSF). We extracted the background from a rectangular region near the edge of the active area of the detector. The XIS detectors were in 1/4 window mode for the observation, and part of the source region falls off of the active region of the detector. We accounted for this when determining the background scaling. We used `xismrfgn` and `xissimrfgn` to produce response matrices, and we combined the XIS0 and XIS3 spectra (the two front-illuminated CCD detectors) into a single file.

For HXD, we analyzed both PIN and GSO data using the Perl scripts `hxdpinxbpi` and `hxdgsoxbpi`, respectively, after screening with the standard selection criteria. These scripts produce deadtime-corrected source and background spectra automatically. The non X-ray background model was taken from the FTP sites²⁴, and cosmic X-ray background (CXB) was also subtracted based on previous *High Energy Astronomy Observatory (HEAO)* observations (Gruber et al. 1999) for PIN. As an energy response, we used `ae_hxd_pinxinome11_20110601.rsp` for PIN and `ae_hxd_gsoxinom_20100524.rsp` with an additional correction file (`ae_hxd_gsoxinom_crab_20100526.arf`) for GSO. The background count rate is significantly higher than the source rate for GSO, but we still clearly detect Swift J1753.5–0127 at a rate of 0.740 ± 0.026 c/s.

3. RESULTS

3.1. Energy Spectrum

We performed all of the spectral fits using the XSPEC v12.8.2 software. For the X-ray spectra, we used instrument response files produced using the HEASOFT software. For the radio, ground-based optical and near-IR, and UVOT,

²⁴ ftp://legacy.gsfc.nasa.gov/suzaku/data/background/pinnxb_ver2.2_tuned/ and ftp://legacy.gsfc.nasa.gov/suzaku/data/background/gsonxb_ver2.6/

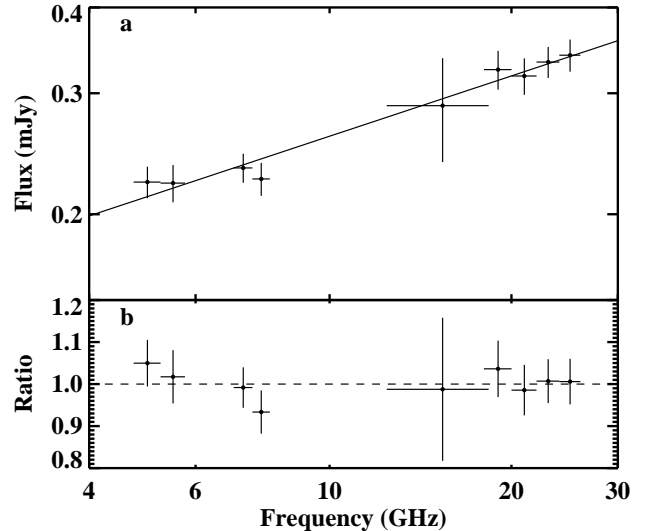


FIG. 3.— (a) Power-law fit to the radio spectrum with $\Gamma = 0.71 \pm 0.05$ ($\alpha = 0.29 \pm 0.05$). The measurements are from VLA (8 points) and AMI (1 point at 15.4 GHz). (b) Data-to-model ratio.

we determined the flux for each data point and then used `flx2xsp` to produce spectral files and unitary response matrices that can be read into XSPEC. All spectral fits are performed by minimizing the χ^2 statistic.

3.1.1. Radio Spectrum

We fitted the radio points with a power-law model (see Figure 3), and this provides an acceptable fit with a reduced- χ^2 (χ^2_ν) of 0.41 for 7 degrees of freedom (dof). The power-law photon index is $\Gamma = 0.71 \pm 0.05$ (90% confidence errors are given here and throughout the paper unless otherwise indicated), and this corresponds to a spectral index of $\alpha = 1 - \Gamma = 0.29 \pm 0.05$ (as mentioned above, α is defined according to $S_\nu \propto \nu^\alpha$, where S_ν is the flux density). We used the XSPEC model `pegpwr1w`, allowing for the power-law normalization to be defined as the flux density at 10 GHz, and we obtain a measurement of $256 \pm 8 \mu\text{Jy}$ at this frequency.

3.1.2. Near-IR to UV Spectrum

The times of the data taken for the near-IR to UV part of the spectrum from Kanata, SLT, and *Swift*/UVOT are shown in Figure 2. The ground-based (Kanata and SLT) observations were taken in five epochs over six nights (see Tables 2 and 3 for the exact times of the exposures). As the source is variable from night-to-night and also on shorter time scales, we used measurements as close to each other in time as possible, while keeping the maximum wavelength coverage. The *Swift* observation occurred between epochs 3 and 4, and we used the points from epoch 3 because the Kanata V- and J-band measurements occurred on the same night. We also used the K_s -band measurement from epoch 1 because the statistical error bar is large enough to account for source variability. We did not include the B-band measurement because UVOT covered the same frequency, and the UVOT measurement was closer in time to the other observations. For each SLT band, several epoch 3 measurements were made, and for the SED, we used the average value. We estimated the uncertainty on these points by calculating the standard deviation of the measurements.

We fitted the near-IR to UV spectrum with a power-law model with extinction. The XSPEC extinction model, `redden`, is based on the Cardelli, Clayton & Mathis (1989) relationship. The fit is poor ($\chi^2_\nu = 10.8$ for 10 dof), strongly over-predicting the K_s -band point. The photon index for the power-law is $\Gamma = 0.2 \pm 0.2$, but we suspect that this is not physically meaningful. A somewhat better fit (although still far from being formally acceptable) is obtained by replacing the power-law with a blackbody (specifically `bbbodyrad`), and this model is a much better match to the spectral slope in the near-IR. If $E(B-V)$ is left as a free parameter, $\chi^2_\nu = 8.0$ for 10 dof, and we find $E(B-V) = 0.54 \pm 0.06$, $kT = 1.9 \pm 0.3$ eV, and a normalization of $R_{\text{km}}/d_{10} = (1.0 \pm 0.1) \times 10^{12}$, where R_{km} is the size of the blackbody in units of kilometers, and d_{10} is the distance to the source in units of 10 kpc. Fixing $E(B-V)$ to 0.45 gives $\chi^2_\nu = 7.8$ for 11 dof (essentially the same quality as the fit with the extinction parameter free), $kT = 1.51 \pm 0.05$ eV, and $R_{\text{km}}/d_{10} = (1.2 \pm 0.1) \times 10^{12}$.

The fit is worse with a multi-temperature disk-blackbody `diskbb` model ($\chi^2_\nu = 13.4$ for 11 dof); however, a significant improvement is obtained if the outer edge of the disk is left as a free parameter. We implemented this by using the `diskir` model (Gierliński, Done & Page 2008, 2009). We turned off the thermalization in the outer disk ($f_{\text{out}} = 0$), and we set the Compton fraction (L_c/L_d) to zero. This model gives $\chi^2_\nu = 3.6$ for 10 dof, and the near-IR to UV spectrum is shown fitted with this model in Figure 4. For the parameters, we obtain $kT_{\text{in}} = 5_{-1}^{+2}$ eV for the temperature of the inner disk and a value of $1.29_{-0.23}^{+0.26}$ for $\log r_{\text{out}}$, where $r_{\text{out}} = R_{\text{out}}/R_{\text{in}}$, and R_{in} and R_{out} are, respectively, the inner and outer radii of the optically thick accretion disk. The `diskir` normalization, which has the same meaning as the `diskbb` normalization ($N_{\text{diskbb}} = (R_{\text{in,km}}/d_{10})^2 / \cos i$, where $R_{\text{in,km}}$ is the inner radius in units of kilometers, d_{10} is the distance to the source in units of 10 kpc, and i is the inclination of the disk) is $N_{\text{diskbb}} = (9_{-5}^{+11}) \times 10^9$. Here, we simply note that this implies a very large inner disk radius. We consider the implications below in detail after using the same model as a component in fitting the full SED.

None of the fits described above are formally acceptable, and there are a few possible reasons for this. Of course, the first possibility is that the spectrum requires a more complex model than those we have tried. Secondly, it is known that there is significant variability in this part of the spectrum (Zurita et al. 2008; Neustroev et al. 2014), and this is also seen in Figure 2. Finally, the largest residuals (see Figure 4) are in the UV where the extinction changes rapidly. Uncertainties in the extinction law and the calibration of the broad UVOT photometric bins could also lead to the large residuals in this part of the spectrum.

3.1.3. X-ray Spectrum

We performed a simultaneous fit to the spectra from all the X-ray instruments with an absorbed power-law model, allowing for different overall normalizations between instruments. To account for absorption, we used the `tbabs` model with Wilms, Allen & McCray (2000) abundances and Verner et al. (1996) cross-sections. As shown in Table 4, the column density is $N_{\text{H}} = (2.01 \pm 0.05) \times 10^{21} \text{ cm}^{-2}$, the power-law photon index is $\Gamma = 1.722 \pm 0.003$, and this simple model provides a surprisingly good fit with $\chi^2_\nu = 1.40$ for 2143 dof. The residuals (see the data-to-model ratio in Figure 5b) do not show any evidence for an iron emission line as might be expected

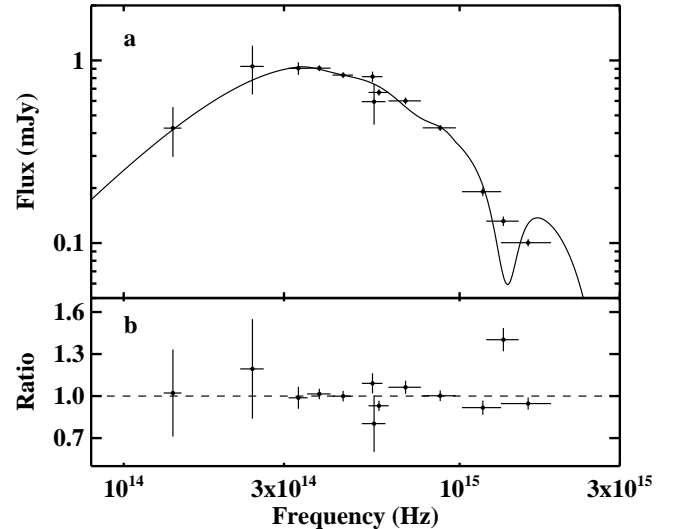


FIG. 4.— (a) Fit to the Kanata, SLT, and UVOT spectra with a multi-temperature disk model with outer radius as a free parameter. The points are not dereddened, and the model assumes $E(B-V) = 0.45$. (b) Data-to-model ratio.

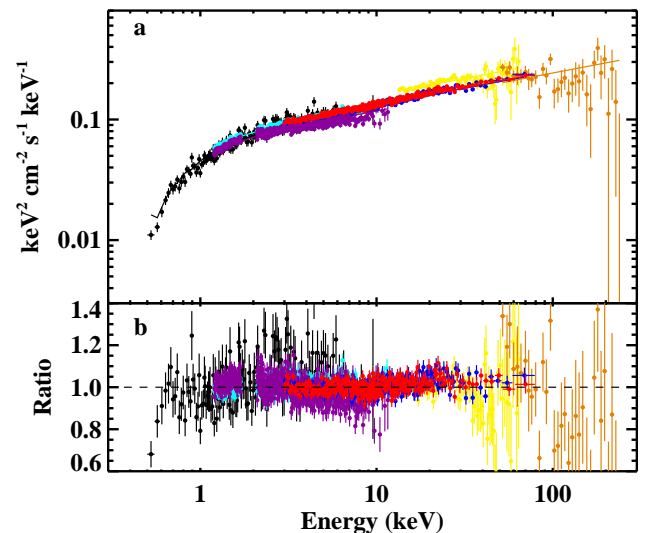


FIG. 5.— (a) Absorbed power-law fit to the Swift J1753.5–0127 X-ray spectrum, including *Swift*/XRT (black), *Suzaku*/XIS03 (cyan), *Suzaku*/XIS1 (purple), *NuSTAR*/FPMA (blue), *NuSTAR*/FPMB (red), *Suzaku*/PIN (yellow), and *Suzaku*/GSO (orange). (b) Data-to-model ratio.

if there was a strong reflection component. For a narrow line in the 6.4–7.1 keV range, the 90% confidence upper limit on the equivalent width is <5 eV, and for a line with a width of 0.5 keV, the upper limit on the equivalent width is <6 eV. The *Suzaku*/GSO shows a different slope above ≈ 80 keV, and we added an exponential cutoff using the `highcut` model. A cutoff with $E_{\text{cut}} = 66_{-10}^{+15}$ keV and $E_{\text{fold}} = 218_{-70}^{+151}$ keV provides a large improvement in the fit to the GSO data, but the overall χ^2_ν only improves to 1.39 for 2141 dof.

Previous work fitting X-ray spectra of Swift J1753.5–0127 has often shown evidence for a thermal disk-blackbody component with an inner disk temperature of $kT_{\text{in}} = 0.1\text{--}0.4$ keV

when the source is in the hard state (Miller, Homan & Miniutti 2006; Hiemstra et al. 2009; Chiang et al. 2010; Reynolds et al. 2010; Cassatella, Uttley & Maccarone 2012; Kolehmainen, Done & Díaz Trigo 2014). Thus, we added a `diskbb` model to the power-law with an exponential cutoff, and the χ^2_ν improves to 1.29 for 2139 dof (see Table 4). While this represents a significant improvement (an F-test indicates that the significance of the additional component is in excess of $12\text{-}\sigma$), the temperature is much higher and the normalization is much lower than previously seen. Our value is $N_{\text{diskbb}} = 3.8^{+1.5}_{-1.1}$ compared to values of $\gtrsim 1000$ reported by Reynolds et al. (2010) and Cassatella, Uttley & Maccarone (2012). A value of $N_{\text{diskbb}} = 3.8$ would imply an unphysically small inner radius. The equation for the inner radius in terms of the gravitational radius is

$$R_{\text{in}}/R_g = (0.676 d_{10} f^2 \sqrt{N_{\text{diskbb}}}) / ((M_{\text{BH}}/M_\odot) \sqrt{\cos i}) \quad , \quad (1)$$

where f is the spectral hardening factor (Shimura & Takahara 1995). For a distance of 3 kpc, $M_{\text{BH}}/M_\odot = 5$, $f = 1.7$, which is a typical value (Shimura & Takahara 1995), and $i = 40^\circ$ based on the estimate of Neustroev et al. (2014), we find $R_{\text{in}}/R_g = 0.26$, which puts the inner radius inside the event horizon.

Figure 5 shows that there is a small deviation from the power-law in the hard X-ray band with the residuals increasing above 10 keV and peaking near 25 keV. Although there is no iron line, this could still be evidence for a weak reflection component or an additional continuum parameter. Adding a reflection component to the power-law using the `relionx` model (Ross & Fabian 2005) provides a significant improvement in the fit to $\chi^2_\nu = 1.27$ for 2138 dof. The reflection covering fraction (determined by calculating the ratio of the 0.001–1000 keV unabsorbed flux in the reflection component to the 0.1–1000 keV unabsorbed flux in the direct component) of $\Omega/2\pi = 0.2$ and the ionization (parameterized by $\xi = L/nR^2$, where L is the luminosity of ionizing radiation, n is the electron number density, and R is the distance between the source of radiation and the reflecting material) of $\xi < 5.3 \text{ erg cm s}^{-1}$ (see Table 4) would both be reasonable for a cool and truncated disk (although we note that low covering fractions can also be explained by beaming emission away from the disk; Beloborodov 1999). The iron abundance of 0.28 ± 0.08 times solar is low but perhaps not unreasonably so. Adding a `diskbb` in addition to `relionx` only provides a small improvement to the fit (to $\chi^2_\nu = 1.26$ for 2136 dof), and N_{diskbb} is even smaller than the previous value. However, it is notable that adding the `diskbb` component causes the iron abundance to change to $0.47^{+0.21}_{-0.15}$ times solar.

3.1.4. XRT Spectrum and the Possibility of a Thermal Component

To investigate further on the question of why we do not see a physically reasonable `diskbb` component while many previous studies of Swift J1753.5–0127 in the hard state did, we fit the X-ray spectra individually. Despite the short exposure time, the *Swift*/XRT spectrum provides the best information on this because it extends down to 0.5 keV without strong instrumental features (we note that *Suzaku*/XIS also has sensitivity down at this energy, but the residuals indicate the presence of instrumental features). A fit to the XRT spectrum with an absorbed power-law model gives $N_{\text{H}} = (2.2 \pm 0.2) \times 10^{21} \text{ cm}^{-2}$, $\Gamma = 1.65 \pm 0.03$, and $\chi^2_\nu = 1.27$ for 131 dof. Adding a `diskbb` provides a significant improvement (to $\chi^2_\nu = 1.17$ for 129 dof), and an F-test indicates a significance

of 99.8% ($3.1\text{-}\sigma$) for the `diskbb` component. The parameters for this fit are $N_{\text{H}} = (5 \pm 1) \times 10^{21} \text{ cm}^{-2}$, $\Gamma = 1.76 \pm 0.06$, $kT_{\text{in}} = 130^{+20}_{-10} \text{ eV}$, and $N_{\text{diskbb}} = (1.6^{+3.0}_{-1.2}) \times 10^5$.

Although the column density is not known precisely, it is clear that it is lower than $\approx 6 \times 10^{21} \text{ cm}^{-2}$. The extinction value that we use in this paper ($E(B-V) = 0.45$) corresponds to $N_{\text{H}} = 3.1 \times 10^{21} \text{ cm}^{-2}$ based on the relationship derived in Güver & Özel (2009). Fixing the column density to this value and fitting the XRT spectrum with a model consisting of a `diskbb` and a power-law gives thermal parameter values of $kT_{\text{in}} = 150^{+30}_{-20} \text{ eV}$ and $N_{\text{diskbb}} = (1.1^{+1.7}_{-0.5}) \times 10^4$. Thus, if we only had the *Swift*/XRT data, we would likely conclude that there is a physically reasonable thermal component. The $kT_{\text{in}} = 150 \text{ eV}$ `diskbb` component that may be present in the *Swift*/XRT spectrum falls rapidly going to energies below soft X-rays and cannot explain the near-IR to UV emission that we see. Thus, even if it is real (and it may not be because it does not appear to be present when fitting all the available data), it is not one of the dominant components in the overall SED, and we do not include it in the following as we build a model for fitting the full SED.

3.1.5. Near-IR, Optical, UV, and X-ray Spectrum

Before fitting the full SED, we fit the near-IR to X-ray spectrum in order to determine if it can be fit in a physically self-consistent manner. As we found that the near-IR to UV spectrum requires a thermal model with the outer disk radius as a parameter, we start by fitting the spectrum with a `diskir` model. While the fits above used a Compton fraction of zero (no Comptonization component), here we allow L_c/L_d to be a free parameter, so that the model includes Comptonization by a thermal distribution of electrons with a temperature of kT_e , causing the model to extend into the X-ray. Within `diskir`, Comptonization is implemented with the `nthcomp` model (Zdziarski, Johnson & Magdziarz 1996; Życki, Done & Smith 1999). The physical scenario being considered is a near-IR to UV thermal component from a truncated optically thick accretion disk, providing seed photons to a Comptonization region with hot electrons.

The `diskir` model alone provides a reasonably good description of the spectrum, but it is not formally acceptable with $\chi^2_\nu = 1.38$ for 2152 dof (see Table 5). The fact that the thermal component acts as the seed photon distribution for the Comptonization emission leads to a somewhat higher value of kT_{in} (12^{+8}_{-5} eV compared to 5^{+2}_{-1} eV found in Section 3.1.2) and a lower normalization, corresponding to a somewhat smaller disk inner radius. The temperature of the Comptonizing electrons is constrained to be $>60 \text{ keV}$, and the Comptonizing fraction is $L_c/L_d = 4.2^{+2.4}_{-2.1}$.

Adding a second continuum component provides a much improved fit, and approximately the same improvement is seen whether we add a power-law with an exponential cutoff or a reflection component (see Table 5). Also, both two-component models lead to very similar values for the thermal component with kT_{in} increasing to 29^{+17}_{-7} eV in one case and $29 \pm 5 \text{ eV}$ in the other. The values of N_{diskbb} decrease further, but they still imply a large disk truncation radius.

The two-component models have very different implications for the properties of the Comptonization region. The physical scenario we are considering in adding an extra power-law is that either this emission comes from the jet or that there is an inhomogeneous or multi-phase Comptonization region (Makishima et al. 2008; Takahashi et al. 2008;

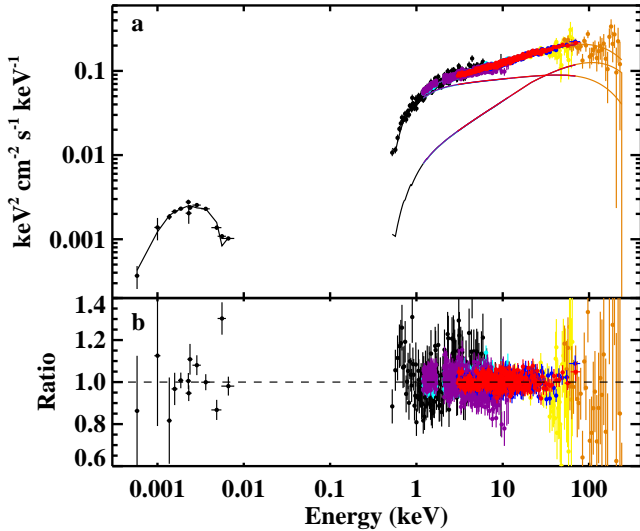


FIG. 6.— (a) Fit to the Swift J1753.5–0127 spectrum, including the data from the near-IR to the X-ray. The model is `diskir` plus a power-law with a high-energy cutoff. The power-law is the harder of the two components. (b) Data-to-model ratio.

Yamada et al. 2013). When this component is added, as shown in Figure 6, its best fit parameters imply a very hard spectrum $\Gamma = 1.33^{+0.08}_{-0.25}$, and it dominates at high energies, so that the `diskir` Comptonization component can have much lower values of kT_e (the constraint is >35 keV) and $L_c/L_d = 0.77 \pm 0.17$. A value of L_c/L_d below 1.0 is unusual for the hard state, but this is due to the fact that much of the hard X-ray flux is in the power-law component.

On the other hand, when reflection is added, as shown in Figure 7, the physical scenario is that the `diskir` Comptonization component is being reflected from the truncated disk. As the `diskir` component must produce the high energy emission in this case, a very high Comptonization temperature is required ($kT_e > 429$ keV) and the Comptonizing fraction increases to $L_c/L_d = 2.4 \pm 0.6$. The `reflionx` parameters are similar to those described above for the X-ray only fits. The ionization state is low, with a value of $\xi = 5.0^{+4.4}_{-2.2}$ erg cm s $^{-1}$. Also, the Fe abundance is 0.33 ± 0.09 , and the covering fraction is $\Omega/2\pi = 0.20$. The ionization parameter and the covering fraction do not seem unreasonable for a cool and truncated disk, but we cannot say with any certainty which two-component model is more likely to be correct.

3.1.6. Full SED

When the full radio to hard X-ray SED is put together, it is immediately clear that the extrapolation of the power-law seen in the radio band is well above the flux measured in the near-IR (even after dereddening). This implies that the radio component, which is attributed to the compact jet, must have a spectral break between the IR and radio bands. Thus, we fit the SED with a model consisting of a broken power-law (`bknpower`) and a `diskir` component. The `bknpower` component provides all of the emission in the radio band, and we fix the power-law index below the break energy (E_{break}) to $\Gamma_1 = 0.7$. The index above the break (Γ_2) is left as a free parameter, and we find that the best fit model has a strong contribution from the `bknpower` above ≈ 20 keV. As described above, the GSO data require a cutoff, and we multiplied the

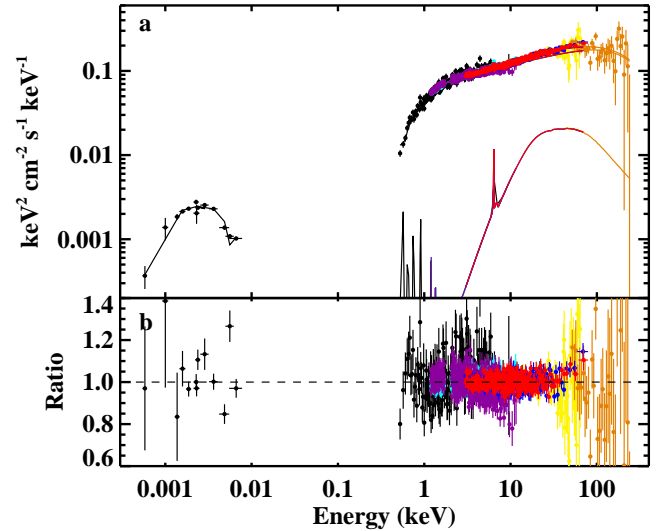


FIG. 7.— (a) Fit to the Swift J1753.5–0127 spectrum, including the data from the near-IR to the X-ray. The model is `diskir` plus a reflection component. (b) Data-to-model ratio.

broken power-law component with a high-energy cutoff.

The continuum components are multiplied by `redden` and `tbabs` as described above. We fixed $E(B-V)$ to 0.45 and N_{H} was left as a free parameter. The fit parameters are given in Table 6, and the quality of the fit is $\chi^2_{\nu} = 1.28$ for 2156 dof. We left the normalizations between the X-ray instruments as free parameters, but we fixed all of the non-X-ray instrument normalizations to the *Swift*/XRT normalization.

We used the XSPEC routine `steppar` to determine the range of possible values for E_{break} . The χ^2 values are nearly constant over a large range, increasing sharply at 1.0×10^{-7} keV (2.4×10^{10} Hz), which corresponds to the highest radio frequency measured, and at 1.5×10^{-5} keV (3.6×10^{12} Hz). At the upper limit, Γ_2 becomes steeper to avoid over-producing in the near-IR, but χ^2 becomes worse because the component no longer extends to the X-ray band. For Figure 8, showing the fitted SED, we set E_{break} to 1.0×10^{-6} keV as an example. The main result is that it is possible for the broken power-law to account for the hard X-ray excess. The `diskir` parameters for the full SED fit (see Table 6) are almost the same as the parameters for the `diskir+highcut*pegpwlw` fits to the near-IR to X-ray fits (see Table 5).

If the hard X-ray excess is explained by a reflection component instead of the broken power-law (i.e., the jet), then Γ_2 could be steeper, allowing for even higher values of E_{break} . We explored this possibility by fitting just the radio to UV spectrum with a modified version of the model shown in Table 6. The modifications include removing `highcut` and fixing the `diskir` components related to Comptonization to the values found for the full SED. In addition, while we allowed Γ_2 to be a free parameter, we did not allow this part of the broken power-law to be steeper than $\Gamma_2 = 2$. While the lower limit on E_{break} is unchanged, the upper limit moves higher, and values as high as $E_{\text{break}} = 6.5 \times 10^{-5}$ keV (1.6×10^{13} Hz) are possible.

3.2. X-ray Timing

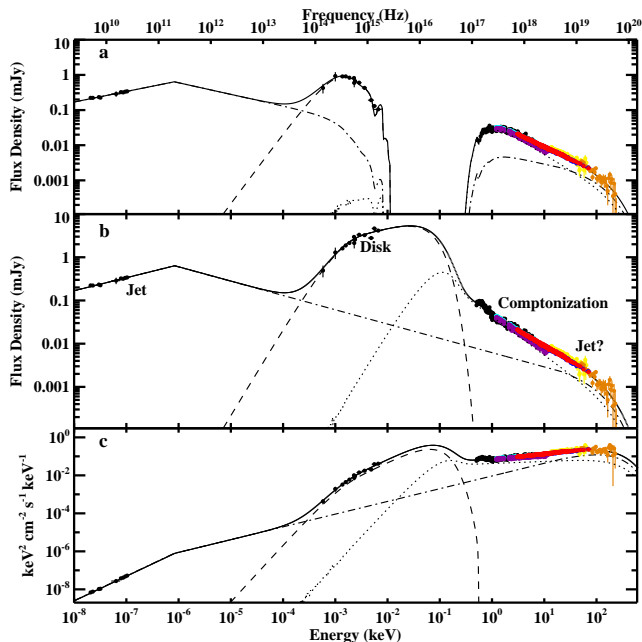


FIG. 8.— (a) The radio to hard X-ray spectral energy distribution for Swift J1753.5–0127. The model is a broken power-law with a high-energy cutoff (dash-dotted line) and a `diskir` component, which we have divided into its thermal component (dashed line) and its Comptonization component (dotted line). The points are not dereddened, and we use $E(B-V) = 0.45$ and $N_{\text{H}} = 2.84 \times 10^{21} \text{ cm}^{-2}$ for the model. The solid line is the sum of the components. (b) The same data and model after dereddening. (c) The same data and model multiplied by energy.

We made power spectra using the *Suzaku*/XIS and *Swift*/XRT data. XIS has a larger effective area and the exposure time is much longer than XRT, so the statistical quality is much better. However, the XRT data are useful because of the higher time resolution. There is good agreement between the two power spectra in the frequency region where they overlap (see Figure 9), but precise agreement is not expected due to the different times being covered and the slightly different energy bandpasses. Thus, we fitted the power spectra separately. For XIS, we used a zero-centered Lorentzian and a power-law at low frequencies. For XRT, the zero-centered Lorentzian is sufficient. The parameters are shown in Table 7, and the fractional rms of the Lorentzians are $27.3\% \pm 0.2\%$ for XIS and $22\% \pm 2\%$ for XRT, which is consistent with the relatively high levels of variability expected for the hard state. The full-width at half-maximum (FWHM) of the Lorentzians are $0.220 \pm 0.005 \text{ Hz}$ for XIS and $0.33 \pm 0.07 \text{ Hz}$ for XRT. In previous work on timing analysis of Swift J1753.5–0127 (Soleri et al. 2013; Kalamkar et al. 2015), the Lorentzian fits were characterized by the frequency where the power spectrum is maximal when plotted as frequency times rms power (ν_{max}) as shown in Figure 9. For XIS and XRT, the values of ν_{max} are $0.110 \pm 0.003 \text{ Hz}$ and $0.16 \pm 0.04 \text{ Hz}$, respectively.

4. DISCUSSION

In this work, we have performed detailed spectral fits to the most complete SED that has been obtained for Swift J1753.5–0127 to date. While previous multi-wavelength studies of this source that included radio measurements have covered the radio, near-IR, optical, and X-ray (Cadolle Bel et al. 2007; Durant et al. 2009; Reynolds et al. 2010; Soleri et al. 2010;

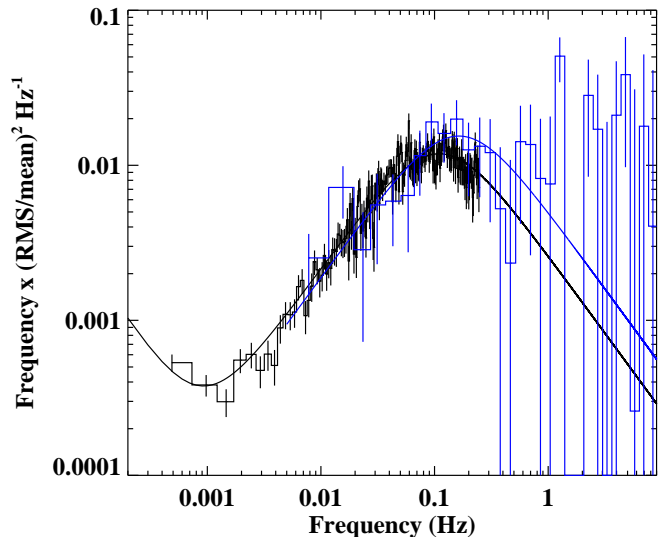


FIG. 9.— Soft X-ray power spectrum from *Suzaku*/XIS (black) and *Swift*/XRT (blue) fitted with a zero-centered Lorentzian and a low-frequency power-law.

Zhang, Yuan & Chaty 2010), we have obtained radio detections at nine frequencies, included UV coverage, and used a combination of seven X-ray spectra, covering 0.5 keV to 240 keV. Here, we discuss three main topics: 1. the implications of the constraint on ν_{break} for the compact jet properties; 2. what we can infer about the properties of the optically thick accretion disk; and 3. the possible origins of the high-energy emission components.

For all these topics, it is useful to estimate the luminosity of Swift J1753.5–0127 during these observations. For the model shown in Figure 8, the absorbed flux over the full energy band covered ($2 \times 10^{-8} \text{ keV}$ to 240 keV) is $1.25 \times 10^{-9} \text{ erg cm}^{-2} \text{ s}^{-1}$. Although there is uncertainty about the break frequency of the broken power-law, this leads to very little uncertainty in the flux since essentially all of the flux is above 1 eV. The unabsorbed flux is $2.71 \times 10^{-9} \text{ erg cm}^{-2} \text{ s}^{-1}$ in the 1 eV to 240 keV band, and this represents the bolometric flux. This is for the model in Table 6, but the unabsorbed flux for the `diskir+reflionx` model shown in Table 5 gives an unabsorbed flux of $2.38 \times 10^{-9} \text{ erg cm}^{-2} \text{ s}^{-1}$ due to the lower column density. Using the average of these two unabsorbed fluxes, the bolometric luminosity is $2.7 \times 10^{36} d_3^2 \text{ erg s}^{-1}$, where d_3 is the distance to the source in units of 3 kpc. For a black hole mass of $5 M_{\odot}$, this corresponds to an Eddington-scaled luminosity of $0.41\% d_3^2 M_5^{-1}$, where M_5 is the black hole mass in units of $5 M_{\odot}$.

4.1. The Compact Jet and the Break Frequency

We are able to obtain a constraint on ν_{break} because of the rising and well constrained radio spectrum ($\alpha = 0.29 \pm 0.05$) along with the fact that the spectrum rises from K_s -band to higher frequencies. Without considering the X-rays, we find that $\nu_{\text{break}} < 1.6 \times 10^{13} \text{ Hz}$ ($\log \nu_{\text{break,Hz}} < 13.2$). If the jet does contribute to the X-rays, then $\nu_{\text{break}} < 3.6 \times 10^{12} \text{ Hz}$ ($\log \nu_{\text{break,Hz}} < 12.6$). A study of 16 ν_{break} measurements or limits for nine black hole systems in the hard state found mostly higher values than the Swift J1753.5–0127 upper limits (Russell et al. 2013a). For the measurements, the me-

dian value of $\log \nu_{\text{break,Hz}}$ is 13.68, and the values range from 12.65 (for XTE J1118+480) to 14.26 (for GX 339–4 and V404 Cyg). When limits are also considered, there are still only two measurements that are as low as the value found for Swift J1753.5–0127: $\log \nu_{\text{break,Hz}} = 12.65 \pm 0.08$ for XTE J1118+480 and < 13.13 for GX 339–4.

While relatively low, the single ν_{break} measurement for Swift J1753.5–0127 does not necessarily indicate anything unusual about the system itself. Multiple measurements of individual systems show significant changes for GX 339–4, XTE J1118+480, MAXI J1836–194, and MAXI J1659–152 (Gandhi et al. 2011; Russell et al. 2013a,b; van der Horst et al. 2013). For GX 339–4, Gandhi et al. (2011) found that ν_{break} changed by a factor of > 10 in less than a day. For MAXI J1836–194, six measurements over a period of less than two months showed changes in $\log \nu_{\text{break,Hz}}$ from close to 11 to close to 14 while the source changed X-ray luminosity and hardness (Russell et al. 2013b, 2014), and the highest value of ν_{break} occurred when the source was at its lowest X-ray luminosity with its hardest X-ray spectrum. The Swift J1753.5–0127 measurements occurred when the spectrum was hard and the X-ray luminosity was low; thus, it may not follow the same trend as MAXI J1836–194. However, this is not surprising since the larger source sample studied in Russell et al. (2013a) did not show any evidence for a correlation between X-ray luminosity and ν_{break} .

In the canonical model for compact jets (Blandford & Königl 1979), the jet spectrum is composed of a superposition of synchrotron components with a continuum of peak frequencies due to changing optical depth. The synchrotron spectrum from each region depends primarily on the magnetic field strength and also on the radial size of the jet. The value of ν_{break} depends on both the magnetic field and the radial size of the jet in its acceleration zone, which is close to the base of the jet. To place constraints on these quantities (B and R), we use equations 1 and 2 from Gandhi et al. (2011), which are based on a single-zone cylindrical approximation (Chaty, Dubus & Raichoor 2011). We estimate the upper limit on B using the parameters from the full SED fit (see Table 6). The input parameters to the equations are $\nu_{\text{break}} < 3.6 \times 10^{12}$ Hz, the flux at 3.6×10^{12} Hz, which is 1.42 mJy, and the slope of the power-law above ν_{break} . To determine the slope, we fixed ν_{break} to 3.6×10^{12} Hz, refit the SED, and found a value of 1.4, which corresponds to $\alpha = -0.4$. The upper limit on the magnetic field strength in the acceleration zone is $B < 2.4 \times 10^3 d_3^{-0.24}$ G and $R > 1.8 \times 10^9 d_3^{0.936}$ cm. If we do not consider the X-rays, $\nu_{\text{break}} < 1.6 \times 10^{13}$ Hz, the flux at 1.6×10^{13} Hz is 2.18 mJy, and the slope of the power-law above ν_{break} is assumed to be 2 ($\alpha = -1$), giving $B < 9.6 \times 10^3 d_3^{-0.21}$ G and $R > 4.6 \times 10^8 d_3^{0.954}$ cm. Also, from the radio alone, we know that $\nu_{\text{break}} > 2.5 \times 10^{10}$ Hz, and the flux at this frequency is 0.34 mJy. Assuming $\alpha = -1$, we derive $B > 18 d_3^{-0.21}$ G and $R < 1.2 \times 10^{11} d_3^{0.954}$ cm.

Two examples of hard state black hole systems for which B and R have been previously calculated using this same technique are GX 339–4 (Gandhi et al. 2011) and MAXI J1836–194 (Russell et al. 2014). For GX 339–4, these quantities were estimated to be $B \approx 1.5 \times 10^4$ G and $R \approx 2.5 \times 10^9$ cm. For MAXI J1836–194, estimates for B and R were obtained for three hard state observations: one during the rise of an outburst and two during outburst decay. Figure 6 of Russell et al. (2014) shows $B \sim 10^2$ G and $R \sim 10^{12}$ cm during the rise and

$B \sim 3 \times 10^{3-4}$ G and $R \sim 10^{9-10}$ cm during the decay. Thus, the ranges of $B = 1.8 \times 10^1 - 9.6 \times 10^3 d_3^{-0.21}$ G and $R = 4.6 \times 10^8 - 1.2 \times 10^{11} d_3^{0.954}$ cm that we derive for Swift J1753.5–0127 are largely consistent with the range of values previously determined for these two sources. The best agreement in the jet properties between Swift J1753.5–0127 and GX 339–4 and MAXI J1836–194 (during decay) occurs if the actual value of ν_{break} for Swift J1753.5–0127 is close to the upper end of the range of possible values.

4.2. The Optically Thick Accretion Disk

Here, we discuss the spectral components that can be modeled as thermal emission and the implications for the optically thick accretion disk. First, we discuss the near-IR to UV component that is consistent with a multi-temperature disk model with $kT_{\text{in}} = 28^{+21}_{-11}$ eV. Then, we consider the possibility of a second thermal component in the soft X-ray band with $kT_{\text{in}} \approx 150$ eV.

Our spectral model assumes that the near-IR to UV emission is strongly dominated by a disk component, and it is worthwhile to consider how secure this assumption is. We know that at least a large fraction of the emission comes from the disk because of the double-peaked emission lines that are seen in this bandpass (Froning et al. 2014; Neustroev et al. 2014; Rahoui et al., submitted to ApJ). However, Neustroev et al. (2014) also find a weak emission line and two weak absorption lines (all three unidentified) in the optical, which they interpret as coming from the companion star. If this interpretation is correct (and we note that the fiducial black hole mass and source distance that we use in this paper depend on it), then it requires some contribution from the companion in the optical. Without X-ray irradiation, the emission from the companion would be negligible: a blackbody with a temperature of 3000 K (Neustroev et al. 2014), a radius equal to the companion’s Roche lobe size of 1.68×10^{10} cm, and a distance of 3 kpc has a flux that is two orders of magnitude lower than the measured flux in the near-IR and three orders of magnitude lower in the optical. Thus, the temperature of the irradiated side of the companion must be significantly hotter for there to be a contribution to the optical flux. However, the crucial point is that even if the three lines are from the companion, they are extremely weak in comparison to the very strong double-peaked lines from the disk, indicating that the disk emission is much stronger than any potential contribution from the companion.

One possibility that we cannot completely rule out is that there are additional components from the compact jet. The broken power-law emission represents the post-shock synchrotron component. While this is the only component that has been seen in SEDs of accreting black holes that is widely accepted as emission from the compact jet, theoretical jet models indicate that pre-shock synchrotron can be relatively bright in the optical and UV (Markoff, Nowak & Wilms 2005; Homan et al. 2005; Migliari et al. 2007; Maitra et al. 2009). Another possibility that has been suggested as a contributor to the optical emission is synchrotron emission from non-thermal electrons in the hot accretion flow (i.e., the corona). A complex optical/X-ray cross-correlation function was reported for Swift J1753.5–0127 (Durant et al. 2008, 2011), and it was shown that it could be explained if the optical emission had components from the disk and the corona (Veledina, Poutanen & Vurm 2011). The coronal contribution to the cross-correlation function has been observed to vary inversely

with the strength of the disk (Hynes et al. 2009). Rahoui et al. (submitted to ApJ) show that Swift J1753.5–0127 had a strong and likely dominant thermal disk component in observations taken a few months after ours²⁵, which would suggest a relatively weak coronal contribution to the optical during our observations.

With the caveats about the possibility of a fractional contribution from pre-shock synchrotron emission or the corona, we can compare the parameters of the thermal near-IR to UV component to previous studies of Swift J1753.5–0127 SEDs where this component has also been modeled as thermal emission (Zhang, Yuan & Chaty 2010; Froning et al. 2014). From Tables 5 (last two columns) and 6, the values of N_{diskbb} are $(5.5_{-3.1}^{+18}) \times 10^7$, $(8.2_{-6.1}^{+72}) \times 10^7$, and $(9.0_{-1.2}^{+89}) \times 10^7$. Using Equation 1, these values imply strongly truncated disks. As before, we assume $M_{\text{BH}} = 5 M_{\odot}$, $d = 3$ kpc, and $i = 40^{\circ}$. To determine the lower limits on the inner disk radii, we assume $f = 1$, and the values are $R_{\text{in}} > 227 R_g$, $> 212 R_g$, and $> 409 R_g$. While previous studies have mostly assumed a larger distance to Swift J1753.5–0127, this would make the values of R_{in} larger. Froning et al. (2014) modeled a near-IR to UV SED and determined that R_{in} needed to be $> 100 R_g$ to avoid overpredicting the simultaneously measured X-ray spectrum. Zhang, Yuan & Chaty (2010) used a self-consistent model with optically thick disk emission, jet emission, and a Comptonization component, and they were able to fit a radio to hard X-ray SED with $R_{\text{in}} = 500 R_g$. Zhang, Yuan & Chaty (2010) assumed different values for d , M_{BH} , and i , and if we recalculate their R_{in} using the values we adopt, the result is $R_{\text{in}} = 350 R_g$. While the precise value of R_{in} is likely to vary in time, all of these measurements suggest that the near-IR to UV component comes from a strongly truncated disk.

The spectral fits also constrain the outer disk radius based on the parameter $\log(R_{\text{out}}/R_{\text{in}}) = 2.31_{-0.04}^{+0.06}$ (see Table 6). For $N_{\text{diskbb}} = 9 \times 10^7$ (the best fit value), we calculate $R_{\text{out}} = 6.6 \times 10^{10}$ cm. We compare this value to the system parameters reported by Neustroev et al. (2014), where they determine that the binary separation is $a \lesssim 1.1 \times 10^{11}$ cm, and the size of the black hole’s Roche lobe is 7.1×10^{10} cm. A filling fraction of 90% is typically assumed for an accretion disk, which would result in a predicted disk size of 6.4×10^{10} cm, which is in excellent agreement with our measurement. Although it will be important to confirm the system parameters with radial velocity measurements of the companion star when the source is in quiescence (if it is bright enough), we see this R_{out} comparison as another piece of evidence that the near-IR to UV component is strongly dominated by emission from the accretion disk.

The 150 eV component is marginally significant in the XRT spectrum, and it is not detected when the XIS data are included. However, for previous observations of Swift J1753.5–0127, the presence of a 0.1–0.4 keV thermal component was well-established from spectral (see references in Section 3.1.3) and timing (Uttley et al. 2011) measurements. Even though our 2014 April observation is at a moderately lower X-ray flux level (only a factor of 2–3 lower than the majority of the previous observations), seeing a weak thermal component in the X-ray band is not surprising. If we use $N_{\text{diskbb}} = 1.1 \times 10^4$ and carry out the same inner radius cal-

ulation as performed for the near-IR to UV component, we obtain $R_{\text{in}} = 5 R_g$ for $f = 1$ and $R_{\text{in}} = 14 R_g$ for $f = 1.7$, suggesting that this component could come from a disk that extends close to the ISCO. The presence of two thermal components in the SED of Swift J1753.5–0127 has been previously reported (Chiang et al. 2010), and potential physical interpretations are discussed in that work. It has been shown that a small inner optically thick accretion disk can form due to condensation of material from the corona (Liu et al. 2007; Meyer, Liu & Meyer-Hofmeister 2007; Taam et al. 2008), and Chiang et al. (2010) consider this possibility as well as a scenario where strong irradiation at the inner edge of a truncated disk distorts the temperature profile. For the inner disk possibility, it has been predicted that the inner disk can exist down to $L/L_{\text{Edd}} \sim 0.1\%$ and then completely evaporate below this level (Taam et al. 2008). Thus, given the luminosity of Swift J1753.5–0127 during our observation ($L/L_{\text{Edd}} \sim 0.4\%$), the presence of an inner disk is predicted.

As previously mentioned, the luminosity at the time of our observation of Swift J1753.5–0127 was close to the lowest level since the source was discovered, but it was only a factor of a few times lower than the highest levels seen over the past several years (see Figure 1). The X-ray power spectrum also suggests that the properties during our observation were at one end of a continuum as opposed to requiring some major overall change in the system. Soleri et al. (2013) report on timing analysis of 67 *Rossi X-ray Timing Explorer (RXTE)* observations of Swift J1753.5–0127 during 2009 and 2010. While the comparison to our observation is somewhat complicated by the fact that most of the *RXTE* observations required two Lorentzian components, fifteen of the power spectra were fitted with a single Lorentzian, allowing for a direct comparison. For those cases, the values of ν_{max} range from 0.18 Hz to 3.18 Hz. Thus, our *Suzaku* and *Swift* measurements of 0.110 ± 0.003 Hz and 0.16 ± 0.04 Hz, respectively, are only slightly lower than the Soleri et al. (2013) measurements.

4.3. The Origin of the X-ray Emission

A major question in recent years concerns how much of the X-ray emission can be attributed to the compact jet. In the model of Markoff, Nowak & Wilms (2005), the jet can produce X-rays via post-shock synchrotron emission, which can be modeled as the broken power-law that we use in our fits, or synchrotron self-Compton (SSC) from the base of the jet, which can contribute in the hard X-ray band. The SEDs of GX 339–4, GRO J1655–40, and XTE J1118+480 allow for the possibility that all the soft X-ray emission comes from the post-shock synchrotron component (Markoff, Nowak & Wilms 2005; Migliari et al. 2007; Maitra et al. 2009). For Swift J1753.5–0127, Figure 8 shows that such a scenario is ruled out, and a Comptonization component is strongly required by the data.

The question of what makes Swift J1753.5–0127 different is directly relevant to the question of what is different about the outliers in the X-ray/radio correlation. Although one possibility is that Swift J1753.5–0127 has a stronger Comptonization component in the X-rays, another possibility is that it has a weaker radio jet. In Section 4.1, we showed that the highest possible peak flux for the Swift J1753.5–0127 broken power-law component is 2.18 mJy. This corresponds to a specific (peak) luminosity of $2.3 \times 10^{19} d_3^2 \text{ erg s}^{-1} \text{ Hz}^{-1}$ at $\nu_{\text{break}} = 1.6 \times 10^{13}$ Hz. Russell et al. (2013a) give 15 peak luminosities for nine hard state black hole systems, and the

²⁵ The Rahoui et al. (submitted to ApJ) observations were made on 2014 August 16 (MJD 56885), and the X-ray light curves shown in Figure 1 do not show any major change between April and August.

values range from 7.1×10^{19} to 1.9×10^{22} $\text{erg s}^{-1} \text{Hz}^{-1}$ with a median value of 1.2×10^{21} $\text{erg s}^{-1} \text{Hz}^{-1}$. Thus, assuming a distance of 3 kpc, the peak jet luminosity for Swift J1753.5–0127 is 50 times lower than the median and 3 times lower than the least luminous system. The distance to Swift J1753.5–0127 would need to be 5–6 kpc to move the Swift J1753.5–0127 peak jet luminosity close to the least luminous system, which is conceivable, but it would need to be ≈ 21 kpc to make the Swift J1753.5–0127 comparable with the median peak jet luminosity, which can be ruled out.

We made a second radio luminosity comparison by integrating the radio power-law measurements for Swift J1753.5–0127 and the black hole sources from Russell et al. (2013a) up to ν_{break} . For Swift J1753.5–0127, the luminosity up to 1.6×10^{13} Hz is $3.1 \times 10^{32} d_3^2 \text{erg s}^{-1}$. For the sources from Russell et al. (2013a), not all 15 of the SEDs are high enough quality to make a reliable luminosity determination. There was sufficient information to calculate ten luminosities for eight sources. These ranged from $1.8 \times 10^{33} \text{erg s}^{-1}$ for XTE J1118+480 and $2.0 \times 10^{33} \text{erg s}^{-1}$ for Cyg X-1 to $1.1 \times 10^{36} \text{erg s}^{-1}$ for GS 1354–64 and $3.1 \times 10^{36} \text{erg s}^{-1}$ for V404 Cyg. The median value is $1.1 \times 10^{35} \text{erg s}^{-1}$, and the distance to Swift J1753.5–0127 is certainly not large enough for the luminosity to approach that value. Thus, the low luminosity radio jet may be at least part of the reason why Swift J1753.5–0127 is an outlier.

While the Swift J1753.5–0127 SED is consistent with Comptonization being dominant at soft X-rays, our results show that multiple components are required to explain the entire 0.5–240 keV X-ray spectrum. In our spectral fits, we considered a reflection component or the post-shock synchrotron component. Figure 7 illustrates the reflection possibility, and such a scenario is consistent with our overall picture for the system. The outer optically thick disk could produce a weak ($\Omega/2\pi = 0.20$) reflection component, and it would be expected to have a low ionization, which is consistent with $\xi = 5.0_{-2.2}^{+4.4} \text{erg cm s}^{-1}$. While an iron line detection would be strong evidence in favor of the reflection interpretation, there is no iron line in the Swift J1753.5–0127 spectrum, but we find that it is possible to explain the lack of an iron line with an iron abundance of 0.33 ± 0.09 of the solar value. This iron abundance may be problematic for the reflection interpretation, but we do not think that it is low enough to rule it out. We have also considered the fact that this is the only model that requires a very high Comptonization temperature ($kT_e > 429 \text{keV}$). This occurs because the reflection component falls at high energies, allowing the overall model to fit the steeper *Suzaku*/GSO spectrum without an exponential cutoff in the direct model. This electron temperature is higher than has been inferred from measurements of other accreting black holes in the higher luminosity parts of their hard states, which are typically in the 50–120 keV range (Poutanen & Veledina 2014, and references therein). However, it is predicted that kT_e should increase to hundreds of keV in the lower luminosity parts of the hard state (Gardner & Done 2013). Thus, the lack of an iron line is the strongest reason to disfavor the reflection possibility, but this scenario is not ruled out.

The model where the hard X-rays are due to post-shock synchrotron emission (see Figure 6) has the advantage of a much more typical electron temperature ($kT_e > 33 \text{keV}$). On the other hand, the slope of the power-law, $\Gamma = 1.33_{-0.25}^{+0.08}$ ($\alpha = -0.33_{-0.08}^{+0.25}$), while not unreasonable for optically thin synchrotron emission, is harder than is seen for other black

hole systems, which have values of α between -0.68 and -1.38 (Russell et al. 2013a). Such a hard spectrum also requires that the spectrum is sharply cutoff to explain the steeper *Suzaku*/GSO spectrum, and the exponential cutoff with $E_{\text{cut}} = 20 \pm 3 \text{keV}$ and $E_{\text{fold}} = 142_{-25}^{+110} \text{keV}$ is probably inconsistent with the more gradual cutoff predicted for a synchrotron spectrum (Zdziarski et al. 2003). A third possibility that was mentioned above but not specifically considered in our spectral modeling is that the extra hard X-ray component is due to SSC emission from the base of the jet. Fits with the Markoff, Nowak & Wilms (2005) compact jet model are beyond the scope of this paper, but it would be interesting to use our SED to test this model in future work.

Finally, we have considered whether any of our conclusions might be affected by day-to-day source variability given that the observations we use for the full SED cover ~ 2.8 days from the K_s -band observation to the VLA observation (although most of the measurements for the SED come from a smaller span of times). Figure 2 shows that there is little day-to-day variability in the optical and near-IR during the campaign, and this is consistent with previous long-term studies of Swift J1753.5–0127 (e.g., Shaw et al. 2013). Also, the *Suzaku*/XIS observations show day-to-day stability in the soft X-ray flux. It is a little less clear whether there are changes in the radio and IR compact jet spectrum as other black hole systems have shown significant changes in the break frequency on time scales of a day as discussed in Section 4.1. We already consider a large range of break frequencies; thus, the conclusions that there is a separate thermal component in the near-IR to UV and that a Comptonization component is required in the soft X-ray should not be affected. However, the question of whether the extra hard X-ray component comes from the compact jet depends very sensitively on the break frequency and spectral slope. To reach a definitive conclusion on the origin of the hard X-ray emission may require simultaneous radio and hard X-ray monitoring.

5. SUMMARY AND CONCLUSIONS

We have obtained radio, near-IR, optical, UV, and X-ray coverage for the long-term black hole transient Swift J1753.5–0127 in 2014 April when the source was in the hard state at one of its lowest X-ray luminosities ($2.7 \times 10^{36} d_3^2 \text{erg s}^{-1}$) since the discovery of the source. We performed fitting of the broadband energy spectrum as well as the X-ray power spectrum. We obtain results concerning the compact jet, the optically thick accretion disk, and the origin of the X-ray emission, which is also relevant for the question of why Swift J1753.5–0127 is a radio/X-ray correlation outlier.

With the combination of the rising radio spectrum, and the rise in the near-IR, ν_{break} is constrained for the post-shock synchrotron component of the compact jet, and this provides constraints on B and R for the jet acceleration zone. While the post-shock synchrotron component may contribute in hard X-rays, the soft X-ray flux is far too high to be part of this component, which we model with a Comptonization component. Based on this result, Swift J1753.5–0127 appears to be an outlier because of the combination of a strong Comptonization component and a jet with peak and broadband luminosities significantly lower than is seen for other black hole systems.

The low jet luminosity and the low extinction for Swift J1753.5–0127 appear to provide an opportunity to clearly see emission components that may be too weak or too absorbed to see in other systems. The double-peaked emis-

sion lines (Froning et al. 2014; Neustroev et al. 2014; Rahoui et al., submitted to ApJ) clearly show that the near-IR to UV spectrum has at least a strong (likely dominant) thermal disk component. Further evidence that the near-IR is dominated by thermal disk emission is that the component can be modeled by a disk with an outer radius of $R_{\text{out}}/R_g = 90,000 d_3 M_5^{-1}$ ($R_{\text{out}} = 6.6 \times 10^{10} d_3 \text{ cm}$), consistent with the expected size of the disk given previous measurements of the size of the companion's Roche lobe. The fact that this component does not contribute in the X-ray band constrains the inner radius to be $R_{\text{in}}/R_g > 212 d_3 M_5^{-1}$. While this implies that the near-IR to UV emission comes from a strongly truncated disk, there is also some evidence for a weak 150 eV thermal component in the soft X-rays, and its inner radius could be as small as 5–14 R_g . The presence of two thermal components could provide support for predictions that low luminosity systems may have inner and outer optically thick disks with a gap in the middle.

Finally, we have considered the possibility that there is a reflection component in the spectrum. In the presence of strong hard X-rays, one expects to see a reflection component from the optically thick material. The hard X-ray spectrum is consistent with the presence of a reflection component, but no iron line is detected. The low ionization ($\xi = 5.0_{-2.2}^{+4.4} \text{ erg cm}^{-2} \text{ s}^{-1}$) and low covering fraction ($\Omega/2\pi = 0.2$) would favor the possibility that this component comes from the outer optically thick disk. If reflection is the cause of the second hard X-ray component, then invoking the jet to explain the extra hard X-ray emission (see Figure 8) may not be required.

We thank the referee for useful comments that helped to improve the manuscript. This work was supported under NASA Contract No. NNG08FD60C, and made use of data from the *NuSTAR* mission, a project led by the California Institute of

Technology, managed by the Jet Propulsion Laboratory, and funded by the National Aeronautics and Space Administration. We thank the *NuSTAR* Operations, Software and Calibration teams for support with the execution and analysis of these observations. This research has made use of the *NuSTAR* Data Analysis Software (NuSTARDAS) jointly developed by the ASI Science Data Center (ASDC, Italy) and the California Institute of Technology (USA). The PS1 Surveys have been made possible through contributions of the Institute for Astronomy, the University of Hawaii, the Pan-STARRS Project Office, the Max-Planck Society and its participating institutes, the Max Planck Institute for Astronomy, Heidelberg and the Max Planck Institute for Extraterrestrial Physics, Garching, The Johns Hopkins University, Durham University, the University of Edinburgh, Queen's University Belfast, the Harvard-Smithsonian Center for Astrophysics, and the Las Cumbres Observatory Global Telescope Network, Incorporated, the National Central University of Taiwan, and the National Aeronautics and Space Administration under Grant No. NNX08AR22G issued through the Planetary Science Division of the NASA Science Mission Directorate. JAT acknowledges partial support from NASA under *Swift* Guest Observer grants NNX13AJ81G and NNX14AC56G. SC acknowledges the financial support from the UnivEarthS Labex programme of Sorbonne Paris Cité (ANR-10-LABX-0023 and ANR-11-IDEX-0005-02), and from the CHAOS project ANR-12-BS05-0009 supported by the French Research National Agency. JMJ is supported by an Australian Research Council (ARC) Future Fellowship (FT140101082) and also acknowledges support from an ARC Discovery Grant. EK acknowledges support from TUBITAK BIDEB 2219 program. This work was supported by the Spanish Ministerio de Economía y Competitividad (MINECO) under grant AYA2013-47447-C3-1-P (SM).

REFERENCES

- Akitaya, H., et al., 2014, Proc. SPIE, 9147, 914740
 AMI Consortium et al., 2012, MNRAS, 423, 1089
 Belloni, T. M., 2010, in Lecture Notes in Physics, Berlin Springer Verlag, ed. T. Belloni, Vol. 794, 53
 Beloborodov, A. M., 1999, ApJ, 510, L123
 Blandford, R. D., & Königl, A., 1979, ApJ, 232, 34
 Blum, J. L., Miller, J. M., Fabian, A. C., Miller, M. C., Homan, J., van der Klis, M., Cackett, E. M., & Reis, R. C., 2009, ApJ, 706, 60
 Bouchet, L., del Santo, M., Jourdain, E., Roques, J. P., Bazzano, A., & DeCesare, G., 2009, ApJ, 693, 1871
 Burrows, D. N., et al., 2005, Space Science Reviews, 120, 165
 Cabanac, C., Fender, R. P., Dunn, R. J. H., & Körding, E. G., 2009, MNRAS, 396, 1415
 Cadolle Bel, M., et al., 2007, ApJ, 659, 549
 Cardelli, J. A., Clayton, G. C., & Mathis, J. S., 1989, ApJ, 345, 245
 Cassatella, P., Uttley, P., & Maccarone, T. J., 2012, MNRAS, 427, 2985
 Chaty, S., Dubus, G., & Raichoor, A., 2011, A&A, 529, A3
 Chiang, C. Y., Done, C., Still, M., & Godet, O., 2010, MNRAS, 403, 1102
 Corbel, S., Coriat, M., Brocksopp, C., Tzioumis, A. K., Fender, R. P., Tomsick, J. A., Buxton, M. M., & Bailyn, C. D., 2013, MNRAS, 428, 2500
 Corbel, S., & Fender, R. P., 2002, ApJ, 573, L35
 Corbel, S., Fender, R. P., Tzioumis, A. K., Nowak, M., McIntyre, V., Durouchoux, P., & Sood, R., 2000, A&A, 359, 251
 Corbel, S., Koerding, E., & Kaaret, P., 2008, MNRAS, 389, 1697
 Corbel, S., Nowak, M. A., Fender, R. P., Tzioumis, A. K., & Markoff, S., 2003, A&A, 400, 1007
 Coriat, M., et al., 2011, MNRAS, 414, 677
 Done, C., & Diaz Trigo, M., 2010, MNRAS, 407, 2287
 Droulans, R., Belmont, R., Malzac, J., & Jourdain, E., 2010, ApJ, 717, 1022
 Durant, M., Gandhi, P., Shahbaz, T., Fabian, A. P., Miller, J., Dhillon, V. S., & Marsh, T. R., 2008, ApJ, 682, L45
 Durant, M., Gandhi, P., Shahbaz, T., Peralta, H. H., & Dhillon, V. S., 2009, MNRAS, 392, 309
 Durant, M., et al., 2011, MNRAS, 410, 2329
 Esin, A. A., McClintock, J. E., & Narayan, R., 1997, ApJ, 489, 865
 Fabian, A. C., et al., 2012, MNRAS, 424, 217
 Fender, R. P., 2001, MNRAS, 322, 31
 Froning, C. S., Maccarone, T. J., France, K., Winter, L., Robinson, E. L., Hynes, R. I., & Lewis, F., 2014, ApJ, 780, 48
 Fürst, F., et al., 2015, arXiv:1506.01381, accepted in ApJ
 Gallo, E., Fender, R. P., & Pooley, G. G., 2003, MNRAS, 344, 60
 Gallo, E., et al., 2014, MNRAS, 445, 290
 Gandhi, P., et al., 2011, ApJ, 740, L13
 Gardner, E., & Done, C., 2013, MNRAS, 434, 3454
 Gehrels, N., et al., 2004, ApJ, 611, 1005
 Gierliński, M., Done, C., & Page, K., 2008, MNRAS, 388, 753
 Gierliński, M., Done, C., & Page, K., 2009, MNRAS, 392, 1106
 Gilfanov, M., & Merloni, A., 2014, Space Sci.Rev., 183, 121
 Grove, J. E., Johnson, W. N., Kroeger, R. A., McNaron-Brown, K., Skibo, J. G., & Philips, B. F., 1998, ApJ, 500, 899
 Gruber, D. E., Matteson, J. L., Peterson, L. E., & Jung, G. V., 1999, ApJ, 520, 124
 Güver, T., & Özel, F., 2009, MNRAS, 400, 2050
 Harrison, F. A., et al., 2013, ApJ, 770, 103
 Hiemstra, B., Soleri, P., Méndez, M., Belloni, T., Mostafa, R., & Wijnands, R., 2009, MNRAS, 394, 2080
 Homan, J., Buxton, M., Markoff, S., Bailyn, C. D., Nespoli, E., & Belloni, T., 2005, ApJ, 624, 295
 Hynes, R. I., Brien, K. O., Mullally, F., & Ashcraft, T., 2009, MNRAS, 399, 281

- Joinet, A., Jourdain, E., Malzac, J., Roques, J. P., Corbel, S., Rodriguez, J., & Kalemci, E., 2007, *ApJ*, 657, 400
- Jonker, P. G., Gallo, E., Dhawan, V., Rupen, M., Fender, R. P., & Dubus, G., 2004, *MNRAS*, 351, 1359
- Jonker, P. G., et al., 2010, *MNRAS*, 401, 1255
- Jourdain, E., Roques, J. P., Chauvin, M., & Clark, D. J., 2012, *ApJ*, 761, 27
- Kalamkar, M., Reynolds, M. T., van der Klis, M., Altamirano, D., & Miller, J. M., 2015, arXiv:1502.01211
- Kalemci, E., Tomsick, J. A., Rothschild, R. E., Pottschmidt, K., & Kaaret, P., 2004, *ApJ*, 603, 231
- Kolehmainen, M., Done, C., & Díaz Trigo, M., 2014, *MNRAS*, 437, 316
- Koyama, K., et al., 2007, *PASJ*, 59, 23
- Laurent, P., Rodriguez, J., Wilms, J., Cadolle Bel, M., Pottschmidt, K., & Grinberg, V., 2011, *Science*, 332, 438
- Liu, B. F., Taam, R. E., Meyer-Hofmeister, E., & Meyer, F., 2007, *ApJ*, 671, 695
- Magnier, E. A., et al., 2013, *ApJS*, 205, 20
- Maitra, D., Markoff, S., Brocksopp, C., Noble, M., Nowak, M., & Wilms, J., 2009, *MNRAS*, 398, 1638
- Makishima, K., et al., 2008, *PASJ*, 60, 585
- Markoff, S., Nowak, M. A., & Wilms, J., 2005, *ApJ*, 635, 1203
- McClintock, J. E., & Remillard, R. A., 2006, *Black hole binaries*, 157–213
- McConnell, M. L., et al., 2000, *ApJ*, 543, 928
- McMullin, J. P., Waters, B., Schiebel, D., Young, W., & Golap, K., 2007, in *Astronomical Data Analysis Software and Systems XVI*, ed. R. A. Shaw, F. Hill, D. J. Bell, Vol. 376, 127
- Meyer, F., Liu, B. F., & Meyer-Hofmeister, E., 2007, *A&A*, 463, 1
- Migliari, S., et al., 2007, *ApJ*, 670, 610
- Miller, J. M., et al., 2010, *ApJ*, 724, 1441
- Miller, J. M., Homan, J., & Miniutti, G., 2006, *ApJ*, 652, L113
- Miller, J. M., Homan, J., Steeghs, D., Rupen, M., Hunstead, R. W., Wijnands, R., Charles, P. A., & Fabian, A. C., 2006, *ApJ*, 653, 525
- Miller, J. M., et al., 2013, *ApJ*, 775, L45
- Miller, J. M., Pooley, G. G., Fabian, A. C., Nowak, M. A., Reis, R. C., Cackett, E. M., Pottschmidt, K., & Wilms, J., 2012, *ApJ*, 757, 11
- Miller, J. M., et al., 2015, *ApJ*, 799, L6
- Neustroev, V. V., Veledina, A., Poutanen, J., Zharikov, S. V., Tsygankov, S. S., Sjöberg, G., & Kajava, J. J. E., 2014, *MNRAS*, 445, 2424
- Palmer, D. M., Barthelmey, S. D., Cummings, J. R., Gehrels, N., Krimm, H. A., Markwardt, C. B., Sakamoto, T., & Tueller, J., 2005, *The Astronomer's Telegram*, 546, 1
- Parker, M. L., et al., 2015, arXiv:1506.00007, accepted in *ApJ*
- Plant, D. S., Fender, R. P., Ponti, G., Muñoz-Darias, T., & Coriat, M., 2015, *A&A*, 573, A120
- Poutanen, J., & Veledina, A., 2014, *Space Sci.Rev.*, 183, 61
- Rahoui, F., Lee, J. C., Heinz, S., Hines, D. C., Pottschmidt, K., Wilms, J., & Grinberg, V., 2011, *ApJ*, 736, 63
- Reis, R. C., Fabian, A. C., & Miller, J. M., 2010, *MNRAS*, 402, 836
- Reis, R. C., et al., 2011, *MNRAS*, 410, 2497
- Reynolds, M. T., Miller, J. M., Homan, J., & Miniutti, G., 2010, *ApJ*, 709, 358
- Rodriguez, J., et al., 2008, *ApJ*, 675, 1449
- Roming, P. W. A., et al., 2005, *Space Sci.Rev.*, 120, 95
- Ross, R. R., & Fabian, A. C., 2005, *MNRAS*, 358, 211
- Russell, D. M., Maitra, D., Dunn, R. J. H., & Markoff, S., 2010, *MNRAS*, 405, 1759
- Russell, D. M., et al., 2013a, *MNRAS*, 429, 815
- Russell, D. M., et al., 2013b, *ApJ*, 768, L35
- Russell, T. D., Soria, R., Miller-Jones, J. C. A., Curran, P. A., Markoff, S., Russell, D. M., & Sivakoff, G. R., 2014, *MNRAS*, 439, 1390
- Sakimoto, K., et al., 2012, *Proc. SPIE*, 8446, 844673
- Schlaflly, E. F., et al., 2012, *ApJ*, 756, 158
- Shaw, A. W., et al., 2013, *MNRAS*, 433, 740
- Shidatsu, M., et al., 2011, *PASJ*, 63, 785
- Shimura, T., & Takahara, F., 1995, *ApJ*, 445, 780
- Skrutskie, M. F., et al., 2006, *AJ*, 131, 1163
- Soleri, P., et al., 2010, *MNRAS*, 406, 1471
- Soleri, P., et al., 2013, *MNRAS*, 429, 1244
- Staley, T. D., et al., 2013, *MNRAS*, 428, 3114
- Taam, R. E., Liu, B. F., Meyer, F., & Meyer-Hofmeister, E., 2008, *ApJ*, 688, 527
- Takahashi, H., et al., 2008, *PASJ*, 60, 69
- Takahashi, T., et al., 2007, *PASJ*, 59, 35
- Tomsick, J. A., Yamaoka, K., Corbel, S., Kaaret, P., Kalemci, E., & Migliari, S., 2009, *ApJ*, 707, L87
- Tonry, J. L., et al., 2012, *ApJ*, 750, 99
- Uttley, P., Wilkinson, T., Cassatella, P., Wilms, J., Pottschmidt, K., Hanke, M., & Böck, M., 2011, *MNRAS*, 414, L60
- van der Horst, A. J., et al., 2013, *MNRAS*, 436, 2625
- Veledina, A., Poutanen, J., & Vurm, I., 2011, *ApJ*, 737, L17
- Verner, D. A., Ferland, G. J., Korista, K. T., & Yakovlev, D. G., 1996, *ApJ*, 465, 487
- Wilms, J., Allen, A., & McCray, R., 2000, *ApJ*, 542, 914
- Yamada, S., Makishima, K., Done, C., Torii, S., Noda, H., & Sakurai, S., 2013, *PASJ*, 65, 80
- Zdziarski, A. A., Johnson, W. N., & Magdziarz, P., 1996, *MNRAS*, 283, 193
- Zdziarski, A. A., Lubiński, P., Gilfanov, M., & Revnivtsev, M., 2003, *MNRAS*, 342, 355
- Zdziarski, A. A., Lubiński, P., & Sikora, M., 2012, *MNRAS*, 423, 663
- Zhang, H., Yuan, F., & Chaty, S., 2010, *ApJ*, 717, 929
- Zurita, C., Durant, M., Torres, M. A. P., Shahbaz, T., Casares, J., & Steeghs, D., 2008, *ApJ*, 681, 1458
- Zwart, J. T. L., et al., 2008, *MNRAS*, 391, 1545
- Życki, P. T., Done, C., & Smith, D. A., 1999, *MNRAS*, 309, 561

TABLE 1
OBSERVING LOG AND EXPOSURE TIMES

| Mission | Instrument | Energy/Filter | ObsID | Start Time (UT) (in 2014) | End Time (UT) (in 2014) | Exposure (s) |
|---------------|------------|---------------|-------------|------------------------------|----------------------------|----------------------|
| Radio | | | | | | |
| VLA | — | 4–8 GHz | — | Apr 5, 11.00 h | Apr 5, 13.00 h | 1518 |
| VLA | — | 18–26 GHz | — | ” | ” | 1746 |
| AMI | — | 12–17.9 GHz | — | Apr 4, 3.07 h | Apr 4, 7.56 h | 16,164 |
| AMI | — | 12–17.9 GHz | — | Apr 5, 2.67 h | Apr 5, 7.64 h | 17,892 |
| Near-IR to UV | | | | | | |
| Kanata | HONIR | $B/V/J/K_s$ | — | Apr 2, 17.3 h | Apr 7, 19.2 h | see text and Table 2 |
| SLT | U42 | $g'/r'/i'/z'$ | — | Apr 3, 9.1 h | Apr 5, 11.0 h | 180 ^a |
| Swift | UVOT | v | 00080730001 | Apr 5, 0.4 h | Apr 5, 5.4 h | 182 |
| Swift | UVOT | b | 00080730001 | ” | ” | 182 |
| Swift | UVOT | u | 00080730001 | ” | ” | 182 |
| Swift | UVOT | $uvw1$ | 00080730001 | ” | ” | 364 |
| Swift | UVOT | $uvm2$ | 00080730001 | ” | ” | 591 |
| Swift | UVOT | $uvw2$ | 00080730001 | ” | ” | 731 |
| X-ray | | | | | | |
| Swift | XRT | 0.5–10 keV | 00080730001 | Apr 5, 0.4 h | Apr 5, 5.4 h | 2,372 |
| Suzaku | XIS0/1/3 | 1.2–12 keV | 409051010 | Apr 3, 17.65 h | Apr 5, 10.69 h | 59,711 |
| NuSTAR | FPMA/B | 3–79 keV | 80002021003 | Apr 4, 21.35 h | Apr 5, 12.69 h | 61,038 |
| Suzaku | HXD/PIN | 13–65 keV | 409051010 | Apr 3, 17.65 h | Apr 5, 10.69 h | 50,434 |
| Suzaku | HXD/GSO | 50–240 keV | 409051010 | Apr 3, 17.65 h | Apr 5, 10.69 h | 50,434 |

^aEach exposure listed in Table 3 was 180 s.

TABLE 2
LOG OF KANATA/HONIR OBSERVATIONS

| Epoch | Filter | MJD | Exposure (s) |
|-------|--------|------------|--------------|
| 1 | V | 56749.7221 | 136 |
| 1 | J | 56749.7232 | 120 |
| 1 | K_s | 56749.7302 | 60 |
| 1 | B | 56749.7405 | 75 |
| 3 | J | 56751.7170 | 120 |
| 3 | V | 56751.7173 | 136 |
| 5 | J | 56754.8052 | 120 |
| 5 | V | 56754.8059 | 136 |

TABLE 3
LOG OF SLT/U42 OBSERVATIONS

| Epoch | Times of g' Exposures (MJD-56750) | Times of r' Exposures (MJD-56750) | Times of i' Exposures (MJD-56750) | Times of z' Exposures (MJD-56750) |
|-------|---|---|---|---|
| 2 | 0.3789 | 0.3806 | 0.3822 | 0.3839 |
| 2 | 0.3856 | 0.3872 | 0.3889 | 0.3905 |
| 2 | 0.3922 | 0.3938 | 0.3955 | 0.3971 |
| 2 | 0.3987 | 0.4004 | 0.4020 | 0.4037 |
| 2 | 0.4054 | 0.4070 | 0.4087 | 0.4103 |
| 2 | 0.4120 | 0.4136 | 0.4153 | 0.4169 |
| 2 | 0.4186 | 0.4202 | 0.4219 | 0.4235 |
| 2 | 0.4252 | 0.4268 | 0.4285 | 0.4301 |
| 2 | 0.4318 | 0.4334 | 0.4351 | 0.4367 |
| 2 | 0.4384 | 0.4400 | 0.4417 | 0.4433 |
| 2 | 0.4450 | 0.4466 | 0.4483 | 0.4499 |
| 2 | 0.4516 | 0.4532 | 0.4549 | 0.4566 |
| 3 | 1.7601 | 1.7578 | 1.7624 | 1.7647 |
| 3 | 1.7695 | 1.7672 | 1.7718 | 1.7741 |
| 3 | 1.7789 | 1.7766 | 1.7812 | 1.7835 |
| 3 | 1.7883 | 1.7860 | 1.7906 | 1.7929 |
| 3 | 1.7977 | 1.7954 | 1.8000 | 1.8023 |
| 3 | 1.8071 | 1.8048 | 1.8094 | 1.8117 |
| 3 | 1.8165 | 1.8142 | 1.8188 | 1.8211 |
| 3 | 1.8259 | 1.8236 | 1.8282 | 1.8305 |
| 3 | 1.8354 | 1.8330 | 1.8377 | 1.8400 |
| 3 | 1.8450 | 1.8428 | 1.8474 | 1.8498 |
| 3 | 1.8545 | 1.8523 | 1.8569 | 1.8592 |
| 3 | 1.8641 | 1.8617 | 1.8664 | — |
| 4 | 2.3799 | 2.3816 | 2.3833 | 2.3849 |
| 4 | 2.3866 | 2.3882 | 2.3899 | 2.3915 |
| 4 | 2.3932 | 2.3948 | 2.3965 | 2.3981 |
| 4 | 2.3998 | 2.4014 | 2.4031 | 2.4047 |
| 4 | 2.4064 | 2.4081 | 2.4097 | 2.4114 |
| 4 | 2.4130 | 2.4147 | 2.4163 | 2.4180 |
| 4 | 2.4196 | 2.4213 | 2.4229 | 2.4245 |
| 4 | 2.4262 | 2.4279 | 2.4295 | 2.4311 |
| 4 | 2.4328 | 2.4345 | 2.4361 | 2.4378 |
| 4 | 2.4394 | 2.4411 | 2.4427 | 2.4444 |
| 4 | 2.4460 | 2.4477 | 2.4493 | 2.4510 |
| 4 | 2.4526 | 2.4543 | 2.4560 | 2.4576 |

TABLE 4
PARAMETERS FOR X-RAY SPECTRAL FITS

| Parameter | Units | pegpwrlw | highecut* pegpwrlw | highecut* pegpwrlw+ diskbb | highecut* pegpwrlw+ reflionx | highecut* pegpwrlw+ diskbb+ reflionx |
|---------------------|---|-------------------|-----------------------|----------------------------------|------------------------------------|---|
| N_{H} | 10^{21} cm^{-2} | 2.01 ± 0.05 | 2.01 ± 0.06 | 2.35 ± 0.11 | 2.60 ± 0.09 | 2.51 ± 0.13 |
| Γ | Photon index | 1.722 ± 0.003 | 1.721 ± 0.003 | 1.699 ± 0.005 | 1.774 ± 0.006 | 1.738 ± 0.015 |
| Flux ^a | $10^{-12} \text{ erg cm}^{-2} \text{ s}^{-1}$ | 253 ± 3 | 253 ± 3 | 253 ± 4 | 254 ± 3 | 253 ± 4 |
| E_{cut} | keV | — | 66_{-9}^{+16} | 60_{-17}^{+12} | 68_{-15}^{+34} | 67_{-12}^{+20} |
| E_{fold} | keV | — | 217_{-72}^{+89} | 209_{-65}^{+568} | >411 | 261_{-95}^{+218} |
| kT_{in} | keV | — | — | $0.67_{-0.05}^{+0.03}$ | — | 0.67 ± 0.06 |
| N_{diskbb} | — | — | — | $3.8_{-1.1}^{+1.5}$ | — | $2.1_{-1.1}^{+1.7}$ |
| ξ | erg cm s^{-1} | — | — | — | <5.3 | <11 |
| Fe/solar | — | — | — | — | 0.28 ± 0.08 | $0.47_{-0.15}^{+0.21}$ |
| N_{refl} | 10^{-4} | — | — | — | $4.1_{-3.3}^{+0.5}$ | $2.2_{-2.0}^{+1.0}$ |
| $\Omega/2\pi$ | — | — | — | — | 0.20 | 0.12 |
| C_{XRT} | — | 1.0 | 1.0 | 1.0 | 1.0 | 1.0 |
| C_{XIS03} | — | 1.06 ± 0.01 | 1.06 ± 0.01 | 1.04 ± 0.01 | 1.04 ± 0.01 | 1.04 ± 0.01 |
| C_{XIS1} | — | 0.97 ± 0.01 | 0.97 ± 0.01 | 0.95 ± 0.01 | 0.95 ± 0.01 | 0.95 ± 0.01 |
| C_{FPMA} | — | 1.08 ± 0.01 | 1.08 ± 0.01 | 1.07 ± 0.01 | 1.06 ± 0.01 | 1.06 ± 0.01 |
| C_{FPMB} | — | 1.10 ± 0.01 | 1.10 ± 0.01 | 1.08 ± 0.01 | 1.08 ± 0.01 | 1.08 ± 0.01 |
| C_{PIN} | — | 1.31 ± 0.02 | 1.31 ± 0.02 | 1.26 ± 0.02 | 1.25 ± 0.01 | 1.25 ± 0.02 |
| C_{GSO} | — | 1.05 ± 0.06 | 1.19 ± 0.08 | 1.14 ± 0.09 | 1.16 ± 0.07 | 1.17 ± 0.08 |
| χ^2/dof | — | 2990/2143 | 2970/2141 | 2751/2139 | 2715/2138 | 2699/2136 |

^aunabsorbed 2–10 keV, power-law only

TABLE 5
PARAMETERS FOR NEAR-IR, OPTICAL, UV, AND X-RAY SPECTRAL FITS

| Parameter | Units | diskir | diskir+ highecut* pegpwrlw | diskir+ reflionx |
|-----------------------|---|------------------------|----------------------------------|------------------------|
| $E(B-V)$ | — | 0.45^a | 0.45^a | 0.45^a |
| N_{H} | 10^{21} cm^{-2} | 2.08 ± 0.05 | 2.83 ± 0.10 | 2.60 ± 0.08 |
| diskir | | | | |
| kT_{in} | eV | 12_{-5}^{+8} | 29_{-7}^{+17} | 29 ± 5 |
| N_{diskbb} | 10^7 | 87_{-36}^{+607} | $8.2_{-6.1}^{+72}$ | $5.5_{-3.1}^{+18}$ |
| Γ | Photon index | 1.734 ± 0.003 | 1.90 ± 0.07 | 1.777 ± 0.006 |
| kT_e | keV | >60 | >35 | >429 |
| L_c/L_d | — | $4.2_{-2.1}^{+2.4}$ | 0.77 ± 0.17 | 2.4 ± 0.6 |
| f_{in} | — | 0.1^a | 0.1^a | 0.1^a |
| r_{irr} | — | 1.1^a | 1.1^a | 1.1^a |
| f_{out} | — | 0.0^a | 0.0^a | 0.0^a |
| $\log r_{\text{out}}$ | $\log(R_{\text{out}}/R_{\text{in}})$ | $1.83_{-0.40}^{+0.06}$ | $2.33_{-0.11}^{+0.29}$ | $2.59_{-0.14}^{+0.34}$ |
| highecut*pegpwrlw | | | | |
| Γ | 2nd Photon index | — | $1.33_{-0.25}^{+0.08}$ | — |
| Flux ^b | $10^{-12} \text{ erg cm}^{-2} \text{ s}^{-1}$ | — | 68_{-42}^{+35} | — |
| E_{cut} | keV | — | 21_{-3}^{+2} | — |
| E_{fold} | keV | — | 151_{-26}^{+63} | — |
| reflionx | | | | |
| ξ | erg cm s^{-1} | — | — | $5.0_{-2.2}^{+4.4}$ |
| Fe/solar | — | — | — | 0.33 ± 0.09 |
| E_{fold} | keV | — | — | >507 |
| N_{refl} | 10^{-4} | — | — | $0.78_{-0.32}^{+0.22}$ |
| $\Omega/2\pi$ | — | — | — | 0.20 |
| C_{XRT} | — | 1.0 | 1.0 | 1.0 |
| C_{XIS03} | — | 1.06 ± 0.02 | 1.04 ± 0.01 | 1.04 ± 0.01 |
| C_{XIS1} | — | 0.97 ± 0.01 | 0.94 ± 0.01 | 0.95 ± 0.01 |
| C_{FPMA} | — | 1.08 ± 0.01 | 1.06 ± 0.01 | 1.07 ± 0.01 |
| C_{FPMB} | — | 1.09 ± 0.01 | 1.07 ± 0.01 | 1.08 ± 0.01 |
| C_{PIN} | — | 1.30 ± 0.02 | 1.25 ± 0.02 | 1.26 ± 0.02 |
| C_{GSO} | — | $1.17_{-0.03}^{+0.06}$ | 1.16 ± 0.07 | 1.23 ± 0.07 |
| χ^2/dof | — | 2963/2152 | 2765/2148 | 2769/2148 |

^aFixed.

^bunabsorbed 2–10 keV, power-law only

TABLE 6
PARAMETERS FOR SED FITS

| Parameter | Units | Value |
|-----------------------|--|---|
| $E(B-V)$ | — | 0.45 ^a |
| N_{H} | 10^{21} cm^{-2} | 2.84 ± 0.11 |
| diskir | | |
| kT_{in} | eV | 28^{+21}_{-11} |
| N_{diskbb} | 10^7 | $9.0^{+89}_{-1.2}$ |
| Γ | Photon index | 1.90 ± 0.02 |
| kT_{e} | keV | > 33 |
| L_c/L_d | — | $0.82^{+0.04}_{-0.19}$ |
| f_{in} | — | 0.1 ^a |
| r_{irr} | — | 1.1 ^a |
| f_{out} | — | 0.0 ^a |
| $\log r_{\text{out}}$ | $\log(R_{\text{out}}/R_{\text{in}})$ | $2.31^{+0.06}_{-0.04}$ |
| highecut * bknpower | | |
| Γ_1 | Below E_{break} | 0.7 ^a |
| Γ_2 | Above E_{break} | $1.33^{+0.10}_{-0.13}$ |
| E_{break} | 10^{-6} keV | 0.1–15 |
| ν_{break} | Hz | $2.4 \times 10^{10} - 3.6 \times 10^{12}$ |
| Normalization | $\text{ph cm}^{-2} \text{ s}^{-1} \text{ keV}^{-1}$ at 1 keV | 64 ± 2 |
| E_{cut} | keV | 20 ± 3 |
| E_{fold} | keV | 142^{+110}_{-25} |
| C_{XRT} | — | 1.0 |
| C_{XIS03} | — | 1.04 ± 0.01 |
| C_{XIS1} | — | 0.94 ± 0.01 |
| C_{FPMA} | — | 1.06 ± 0.01 |
| C_{FPMB} | — | 1.07 ± 0.01 |
| C_{PIN} | — | 1.25 ± 0.02 |
| C_{GSO} | — | 1.16 ± 0.07 |
| χ^2/dof | — | 2768/2156 |

^aFixed.

TABLE 7
PARAMETERS FOR POWER SPECTRUM FITS

| Parameter | Units | Value |
|---|-------------|--------------------|
| <i>Suzaku</i> (Lorentzian plus power-law) | | |
| ν_{max} | Hz | 0.110 ± 0.003 |
| rms_{Lor} | — | $27.3\% \pm 0.2\%$ |
| Power-law index | — | 2.12 ± 0.05 |
| rms_{pl} | 0.0001–1 Hz | $4.4\% \pm 1.4\%$ |
| χ^2/dof | — | 284/191 |
| <i>Swift</i> (Lorentzian) | | |
| ν_{max} | Hz | 0.16 ± 0.04 |
| rms_{Lor} | — | $22\% \pm 2\%$ |
| χ^2/dof | — | 51/42 |